Nebular thermal processing of accretionary fine-grained rims in the Paris CM chondrite

Pierre-Marie Zanetta, Hugues Leroux, Corentin Le Guillou, B. Zanda, R.H. Hewins

▶ **To cite this version:**

Pierre-Marie Zanetta, Hugues Leroux, Corentin Le Guillou, B. Zanda, R.H. Hewins. Nebular thermal processing of accretionary fine-grained rims in the Paris CM chondrite. Geochimica et Cosmochimica Acta, 2021, Geochimica et Cosmochimica Acta, 295, pp.135-154. 10.1016/j.gca.2020.12.015 . hal-03135750

HAL Id: hal-03135750
https://hal.univ-lille.fr/hal-03135750

Submitted on 26 Feb 2021

HAL is a multi-disciplinary open access archive for the deposit and dissemination of scientific research documents, whether they are published or not. The documents may come from teaching and research institutions in France or abroad, or from public or private research centers.

L'archive ouverte pluridisciplinaire **HAL**, est destinée au dépôt et à la diffusion de documents scientifiques de niveau recherche, publiés ou non, émanant des établissements d'enseignement et de recherche français ou étrangers, des laboratoires publics ou privés.

Nebular thermal processing of accretionary fine-grained rims in the Paris CM chondrite

P-M. Zanetta[1,2], H. Leroux[1], C. Le Guillou[1], B. Zanda[2,4], R. H. Hewins[2,3]

1. Univ. Lille, CNRS, INRAE, Centrale Lille, UMR 8207 - UMET - Unité Matériaux et Transformations, F-59000 Lille, France. 2. IMPMC, Sorbonne Université, MNHN, UPMC Paris 06, UMR CNRS 7590, 75005 Paris, France. 3. EPS, Rutgers Univ., Piscataway, NJ 08854, USA; 4. Observatoire de Paris, IMCCE, 75014 Paris, France

Research Data repository: ZANETTA, Pierre-marie (2020), "Rim Paris meteorite", Mendeley Data, v1
http://dx.doi.org/10.17632/3dgyytjbp2.1

Keywords: *Chondrites, Fine-grained rims, Matrix, Amorphous silicates, ACADEMY*

Abstract

Fine-grained rims (FGRs) are ubiquitous in chondrites. They consist of unequilibrated mineral assemblages that surround chondrules and refractory inclusions. As such, they carry information about the material that was accreted onto chondrules. To decipher the nature and the formation mechanism of FGRs and compare them to adjacent matrix material, we investigated their composition, mineralogy, density and texture in the pristine Paris CM chondrite. We coupled a new method (ACADEMY; Zanetta et al., 2019) at the scanning electron microscope (SEM) scale that allows high-resolution quantitative petrology and an analytical transmission electron microscope (TEM) study. Significant differences in modal abundance, grain size and porosity are observed between the FGRs and their adjacent matrix. Domains of amorphous silicates with embedded nanosulfides indicate a high degree of preservation. They are less abundant in the matrix than in the rims. In contrast, secondary alteration phases (phyllosilicates, carbonates and tochilinites) are more abundant in the matrix and associated with larger and fewer sulfide grains. The similar composition of the amorphous silicate in the rims and the matrix attests for a close relationship between the two reservoirs. However, matrix underwent more aqueous alteration. We interpret it as the result of the accretion of material with a higher amount of water in the matrix, leading to a more aqueously altered microenvironment. We also find that coarse-grained anhydrous silicates (olivine and pyroxene) are present in the matrix but not in the FGRs, likely as a result of a chondrule fragmentation episode that occurred after FGR but before matrix accretion. Most of the time, FGRs display distinct inner and outer layers. The inner part is compact and displays larger sulfide grains than the outer part, which is more porous (porosity ~ 45%) and altogether more pristine. These mineral and textural differences are not easily explained by differential aqueous alteration. Instead, a pre-accretion thermal process that preferentially affected the inner rim could have induced loss of porosity, compaction of the amorphous silicate domains as well as sulfides growth. We therefore suggest that FGRs acquired their characteristics in the nebula before matrix accretion to form Paris parent body and discuss possible mechanisms such as dust heating in the chondrule formation environment or secondary heating episode of the previously rimmed chondrule as well as gas friction in high-speed collision conditions.

1. Introduction

Chondrites are made of components showing a wide range of formation conditions. Chondrules, metal grains and calcium aluminum inclusions (CAIs) formed at high temperature, while the fine-grained matrix in which they are embedded contains low temperature material, including hydrated silicates and organic compounds as well as abundant volatile elements. The origins and the mixing processes of the high and the low-temperature reservoirs are still poorly understood and several models of accretion have been proposed (Liffman and Toscano, 2000; Laibe et al., 2008; Morbidelli et al., 2012; Gonzalez et al., 2015; Johansen et al., 2015a; Johansen et al., 2015b; Gonzalez et al., 2017; Pignatale et al., 2018; Liffman, 2019).

Located at the interface between the high-temperature components and the matrix, the fine-grained rims (FGRs) in carbonaceous chondrites consist of an unequilibrated fine-grained (≤ 1 µm) assemblage with variable amounts of Mg-Fe amorphous silicates and phyllosilicates which embed anhydrous silicates, sulfides, metal and organic compounds (Brearley, 1993; Zolensky et al., 1993; Lauretta et al., 2000; Zega and Buseck, 2003; Chizmadia and Brearley, 2008). FGRs and matrix are made of a similar phase assemblage but nevertheless exhibit different textures (grain size, compaction, porosity) as well as different presolar grain abundances (Leitner et al., 2016; Haenecour et al., 2018). They might therefore have accreted a similar type of material, which was processed under different conditions (Hanowski and Brearley, 2000; Zega and Buseck, 2003; Chizmadia and Brearley, 2008; Leitner et al., 2016). Metzler et al. (1992) suggested that FGRs formed by the accretion of hydrous phases onto chondrules and named them “accretionary dust mantles “. Other authors proposed that FGRs formed in a parent body by preferential alteration at the chondrule/matrix interface (Sears et al., 1993; Tomeoka and Tanimura, 2000; Trigo-Rodriguez et al., 2006; Takayama and Tomeoka, 2012; Tomeoka and Ohnishi, 2014) or, alternatively, by compaction of dust around chondrules in a regolith (Sears et al., 1993; Takayama and Tomeoka, 2012). Aqueous alteration/metamorphism of FGRs initially made of anhydrous material on a meteorite parent body after nebular accretion was also proposed (Brearley and Geiger, 1991; Zolensky et al., 1993; Hanowski and Brearley, 2001; Hua et al., 2002). The accretional origin is the most likely mechanism and is supported by petrographic evidence of higher abundances of presolar grains in the FGRs as well as by fabric studies (Bland et al., 2011; Leitner et al., 2016; Haenecour et al., 2018). In an accretionary scenario, FGRs carry crucial information on the physical accretion conditions. Two regimes of kinetics have been proposed. Usually, FGRs are considered to be formed with dust collision speeds of order of tens of centimeters per second (Chokshi et al., 1993; Dominik and Tielens, 1997; Cuzzi, 2004; Blum and Wurm, 2008). Other authors argue that slow speed particle collisions produce a dust rim that is far too porous in comparison to what is observed in the different groups and proposed an alternative scenario, the Kinetic Dust Aggregation (KDA) model, where FGRs are formed through relatively high-speed (order of meters per second to kilometers per second) collisions (Liffman and Toscano, 2000; Liffman, 2019). Careful microscale study of the FGRs should bring new insights on the speed collision.

Two major obstacles must be overcome in order to understand the conditions of FGR formation: (1) parent body aqueous alteration and/or thermal metamorphism must be evaluated in order to identify the FGR secondary modification; (2) quantitative characterization of the chemistry, mineralogy and texture is required and is at present challenging due to the sub-micrometer grain size. Previous work includes mineralogical and chemical study by bulk electron probe micro-analysis (EPMA), qualitative SEM-EDX analysis and a number of transmission electron microscopy (TEM) studies (Brearley, 1993; Zolensky et al., 1993; Lauretta et al., 2000; Zega and Buseck, 2003; Chizmadia and Brearley, 2008).

However, spatially resolved analysis of large and representative areas has never been satisfactorily achieved so far.

To overcome these obstacles, we studied a minimally altered chondrite and applied an analytical method that we recently developed. We studied the Paris CM chondrite, which is the least altered of its group (CM2.7-2.9) (Hewins et al., 2014). Paris has the advantage of exhibiting two lithologies showing different alteration degrees and contains highly pristine areas (Marrocchi et al., 2014; Hewins et al., 2014; Leroux et al., 2015; Vinogradoff et al., 2017; Piani et al., 2018). Comparing these two lithologies (referred to hereafter as "least altered" vs "more altered ") allowed us to evaluate the impact of alteration processes on FGRs. To quantify the mineralogy, chemistry and density of sub-micrometric assemblages, FGRs and their adjacent matrix were characterized using the ACADEMY method (Zanetta et al., 2019). This approach combines high resolution SEM and phase mapping, quantitative EPMA and density measurements, which altogether allow us to retrieve the bulk composition of a matrix region. In order to obtain complementary information at the nanometer scale, several representative FGRs and their adjacent matrix were also studied by TEM.

2. Analytical methods

2.1 Scanning electron microscopy (SEM)

We worked on a polished thick section of the CM chondrite Paris 4029-SP6 (Muséum National d'Histoire Naturelle - MNHN, Paris). High-resolution images and hyperspectral maps were acquired using a FEG-SEM JEOL JSM-7800F LV at the University of Lille. The microscope is equipped with an EDX/EBSD Aztec system from Oxford Instruments and a silicon drift detector (SDD) XMaxN of 80 mm^2. Secondary electron (SE) and backscattered electron (BSE) images were collected to identify chondrules, CAIs, metal grains, matrix and FGRs. We used a BSE image mosaic and the Qgis® software to measure their characteristics (FGR thickness, surface area, grain size distribution). More altered and least altered areas of Paris were identified based on chondrule metal grain abundance and the BSE contrast of the matrix (altered areas are less porous and richer in tochilinite-cronstedtite intergrowth (TCI), resulting in brighter contrast). We then acquired four EDX hyperspectral maps at an acceleration voltage of 6 keV to optimize the spatial resolution. Each map consists of a matrix of 1024 by 832 pixels corresponding to a region of 238 µm by 193 µm (pixel size = 230 nm). A working distance of 10 mm and an EDX energy range of 10 keV for 2048 channels were used (5 eV per channel).

In order to study the geometry and the shape of the small (<4 µm) anhydrous silicates (olivine and pyroxene), we also collected higher resolution EDX maps (1024x832 pixels) and BSE images (4096x3328 pixels) corresponding to a 92x80 µm area with pixel sizes of 80 nm and 20 nm. We isolated these anhydrous silicate grains on the BSE images using contrast thresholding and we used the EDX data to check that the selected pixels were anhydrous silicates (olivine or pyroxene).

2.2 Electron probe micro-analysis and bulk composition of phase maps

Chemical compositions were obtained using a CAMECA SX 100 at the University of Lille, at an accelerating voltage of 15 keV, an intensity of 10 nA and a counting time of 20 seconds. A 3 µm wide beam was used for carbonates and phyllosilicates. X-ray peak intensities were collected on TAP, LiF and LPET crystals.

2.3 Transmission electron microscopy (TEM)

Seven electron-transparent sections were prepared using the focused ion beam (FIB) technique with an FEI Strata dual beam 235 (Institute of Electronics, Microelectronics and Nanotechnology, University of Lille). The sections were typically 20x8 µm² in size and 100 nm thick. Each FIB section consisted of two electron-transparent juxtaposed windows of 7-8 µm (~60 µm²) obtained by keeping a 1 µm wide thicker bar in the middle of the foil. This prevented the bending of the section. The FIB sections were studied with an FEI Titan Themis, operating at 300 kV and equipped with a high angular annular dark field (HAADF) detector and a four quadrant, windowless, super-X SDD system (University of Lille). Hyperspectral maps of ~15x7 µm were acquired with a ~ 600 pA current, a dwell time of 2 µs, a probe of several nm, and a duration of ~14 h. They were binned into maps with 15 nm, 50 nm and 100 nm pixel size depending on the spatial resolution requirements (i.e grain size distribution, phase maps or quantification procedure respectively). Compositions were calculated using the Cliff-Lorimer method (Watanabe and Williams, 2006) and an absorption correction procedure (Le Guillou et al., 2018). Experimentally determined k-factors were obtained for the major elements O, Fe, Mg, Al, S, Ca, and K on fayalite, forsterite, basalt, rhyolite, serpentine, wollastonite and pyrite mineral standards.

2.4 ACADEMY methodology

The phase maps were obtained using the ACADEMY methodology (Zanetta et al., 2019) based on the XMapTools and Hyperpsy software (Lanari et al., 2014; de la Peña et al., 2019). High-resolution EDX maps are turned into phase maps using cluster analysis. One spectrum per phase is then identified. In regions where mixing occurs at the sub-pixel size, these reference spectra are used as inputs for “multiple linear least squares” (MLLS) fitting in order to estimate the mixing proportions of the different phases in each pixel. Based on the phase map, we quantified the grain size and shape distribution as well as the grain abundances. Estimated modal abundances were obtained by assuming that grains were sufficiently small and randomly distributed so that their surface area might be converted into a volume. Size distributions were considered only for grain size greater than 1 µm to avoid biases due to pixel size. Density was measured through modeling of the background of the EDX spectra. Background modelling requires to account for absorption in the material. The theoretical expression of the absorption comprises the “mass depth” term “ρx” which is a proxy of the density (see Zanetta et al., 2019). The model was fitted to the experimental data (with ρx as a free parameter). To obtain the density, calibration based on phases of known densities (i.e. olivine, pyroxene, metal grain, sulfide and epoxy) was performed.

Each mineral composition was then quantified with EPMA (point analysis). The bulk compositions of the mapped areas were eventually determined as the combination of the modal abundance (extracted from the phase maps), the density and the composition of individual phases acquired with the EPMA.

3. Results

3.1 Occurrences of FGRs: large scale description

All types of high temperature components (chondrules, CAIs, metal grains) may be surrounded by FGRs (Fig. 1). FGRs occur mostly as darker material in BSE images in comparison to the adjacent matrix. The interface between the matrix and the FGR material is sharp.

In the least altered lithology of Paris, we analyzed a 30 mm^2 area using the Qgis® software. We counted 1202 coarse-grained components (chondrules, chondrule fragments, metal grains and CAI – see supplementary material 1), which represent 34% of that area, while the matrix accounts for 60 % of it and the rims for 6%. These estimations are consistent with previous results (Hewins et al., 2014). Overall, ≈ 80% of the complete chondrules (excluding fragments) display a FGR (Table 1). FGRs are more frequent around large (radius > 80 µm) and regularly shaped (round, smooth boundaries) type I chondrules. The lower value obtained for metal grains (≈ 40%) is likely due to the difficulty to determine whether each grain was an independent component from the start or resulted from the fragmentation of a type I chondrule, since the metal grains are generally round homogeneous objects. Below 80 µm, high temperature components are likely fragments. As already observed by Metzler et al. (1992), fragments exhibit FGRs on one side only.

Relationship between components and FGR sizes

There is a positive correlation between rim thickness and component radius (Fig. 2), which shows that smaller objects exhibit thinner FGRs, independently of their nature. As our measurements are based on 2D SEM images, the resulting truncated chondrule size and rim thickness could explain part of the data deviation around the regression line (R^2=0.55) (Hanna and Ketcham, 2018)). The slope of the regression line (a = 0.14) is lower than that found by (Metzler et al., 1992) and (Trigo-Rodriguez et al., 2006) (~ 0.32 - 0.40), indicating a lower thickness increase as a function of the chondrule size. Metal grains, which exhibit smaller sizes in comparison to the type I chondrules, also exhibit smaller FGRs (mean thickness = 10 µm vs 21 µm for type I chondrules, sup. mat. 1)

FGRs vs matrix in the altered and less altered lithologies

At the interface with the matrix, the rim is darker due to a higher porosity (Fig. 3a). Patches of TCI are often concentrated at this interface forming a brighter layer (Fig. 3b), as already noted by (Hewins et al., 2014). Some of the larger rims have a bilayer structure (~12% of the FGRs of the section, Fig. 3a). At the chondrule interface, the rim appears more compact. The contact between the two layers is sometimes delimited by a fracture (Fig. 3a) but more compact zones sometimes overlap this delimitation (Fig. 3c). In the following, we name these two layers the 'inner' and 'outer' rims. The inner rim is always discontinuous and never surrounds the chondrule entirely, while the outer rim is thicker and surrounds the entire chondrule. In some cases, the inner rims are confined to recesses within the chondrule with a depth of 20-30 µm (Fig. 3a). The inner rim is thus thicker where the chondrule displays a depressed area and thinner elsewhere (Hanna and Ketcham, 2018). Consequently, the inner rim gives a more rounded aspect to the chondrule, whereas the outer rim has a more constant thickness. When rims are not sub-divided, the observed texture is close to that of an outer rim.

In the more altered lithologies of the chondrite, the FGR boundaries are less well-defined (Fig. 3d). The BSE contrast of the FGRs is more homogeneous and the inner and outer rims cannot be distinguished

(Fig. 3e). The material appears brighter in BSE and more compact (Fig. 3f). Figure 3d also shows that chondrules in the altered lithologies display clear embayments that are deeper (50-100 µm; orange arrows) than the recesses observed in the least altered lithology. The BSE images display a gradually brighter contrast near the chondrule in these embayments. Frequent patches of TCI are present in the FGRs (Fig. 3e,f), which was not the case in the least altered lithology.

Matrix in both types of lithologies appears brighter in BSE contrast due to the presence of TCI patches and contains large anhydrous silicate and sulfide grains. In the least altered lithology, patches of "fresh matrix" that are porous, darker and rich in nano-sulfides, are still visible in between TCI patches and coarsely crystalline phyllosilicates. These islands of "fresh areas" display a similar BSE contrast and a similar porosity to those of outer rims. In the more altered lithology, these fresh areas are replaced by abundant TCI increasing the global BSE contrast. These patches of TCI are also larger and richer in S (brighter in Z contrast, see Fig. 3f).

3.2 Petrography and density of the FGRs and the adjacent matrix

The present study is focused on the least altered lithology of Paris, while the more altered lithology was also investigated to document the evolution of the FGRs due to aqueous alteration. We aquired several SEM-EDX phase maps at different locations in the section.

Phase mapping and modal abundances

We studied 4 representative rimmed type I and type II chondrules (Fig. 4). Matrix and rims display similar phases, but their modal abundances differ significantly. The most abundant phase is very fine-grained and has a composition that differs from that of pyroxene and of olivine. At the SEM scale, it is not possible to identify this phase, which might be amorphous silicates, phyllosilicates -or both, mixed with nanoparticles of sulfides. This material represents 87 ± 9 vol. % of the matrix, 90 ± 9 vol. % of the outer rim and 94 ± 10 vol. % of the inner rim (supplementary material 2). An S-rich tochilinite and an Al-rich cronstedtite endmembers of TCI were identified (supplementary material 3; respectively labeled as TCI-T and TCI-C in Fig. 4 & 5). TCI-T is always more abundant in the matrix (6.7 ± 0.5 vol. %) than in the FGRs (2.6 ± 0.2 vol. % in the outer rim and 1.2 ± 0.1 vol. % in the inner rim). Similar abundance trends were found for TCI-C, as well as carbonates and sulfates (Fig. 5), which are almost absent from the rims. TCI generally forms patches of 10 to 20 µm but it can also be found as smaller grains intermingled with the amorphous silicate/phyllosilicate material. Patches of carbonate and sulfate are 5 – 15 µm in size.

Size distribution of anhydrous silicates

Anhydrous silicates (olivine and pyroxene) display a wide range of sizes (from 1 to 100 µm). To analyze the whole range, we coupled a BSE mosaic (with 1 µm/pixel) with EDX phase maps (250 nm/pixel; supplementary material 4). To identify anhydrous silicates on BSE images, we used the BSE intensity of the Mg-end members (Fo>90 and En>90), because they represent the main fraction of the anhydrous silicates (≈ 90 %). The grain size distribution is bimodal (Fig. 6a). The larger fraction has a mean size of ≈ 10 µm and a mode position at ≈ 6 µm while the mean size and the mode of the smaller-sized population falls below 1 µm. The larger population of anhydrous silicates (> 4 µm) is only present in the matrix and not in the FGRs (Fig. 6b). The size distribution of the smaller population is identical for both FGRs and matrix. The grains in both populations are relatively rounded (mean circularity is ~0.8). We applied a threshold on the larger grains (> 4 µm), which are only present in the matrix. We then compared the

relative modal abundance of the smaller population (Fig. 6c-d). Anhydrous silicates grains inferior to 4 µm are more abundant in the outer rim (3.58 ± 0.07 vol.%), whereas the inner rim has 50% less (1.94 ± 0.05 vol.%) and the matrix is intermediate (2.69 ± 0.04 vol.%).

Shape factors were extracted from the high-resolution BSE images (20 nm/pixel). They include the circularity, the aspect ratio, the roundness and the solidity of the grains (supplementary materials 5). We found no correlation between shape factors, the location of the grains and their compositions. For instance, the anhydrous silicates do not exhibit any enrichment in iron as a function of the grain size/shape/or location.

Density maps

We measured the apparent density (including porosity) of amorphous silicate/phyllosilicate groundmass mixed with nanosulfides (Fig. 7). The probed depth is less than 300 nm. The outer rim exhibits the lowest apparent density 2.41±0.18 g/cm^3 whereas the inner rim and the matrix have similar apparent densities of ~2.7±0.21 g/cm^3. This difference in density between the outer rim and the inner rim and matrix is significant and cannot be satisfactorily explained by the modal abundances of the phases alone. It is likely to result from a variation in porosity.

Estimated by MLLS fitting (see section 2.4), a nominal density map was constructed using a mixture made of amorphous silicates/phyllosilicates with a density of ~2.9 g/cm^3 and a varying proportion of nanosulfides (4.6 g/cm^3). The nominal density map was compared to the apparent density map. Using this first order estimate, we deduced two porosity profiles (Fig. 8) by assuming the difference in density to be due either to empty voids or to pores filled by epoxy (1.3 g/cm^3). A higher porosity was found in the outer rim (~ 25-40%) than in the inner rim (~ 20-30%) in both cases.

3.3 Bulk chemical compositions

The average compositions of the mapped areas are comparable for most elements (Fig. 9). Significant variations are observed only for Ca and P in the matrix and K, Na in the rims. Except for these two elements (K and Na), inner and outer rim compositions are similar, while matrix is richer in Fe, Al, Ca and P. The main carriers of Ca and P are carbonate and phosphate, which are present in the matrix (Supplementary material 2) but almost absent from the rims. The difference in Fe is mainly linked to the proportion of TCI in the matrix. Minor elements such as Ti, Cr, K and Na are mainly carried by the silicate groundmass whose composition is more difficult to assess at the SEM scale.

3.4 TEM of FGRs and their adjacent matrix

General observations and porosity measurements

FIB sections extracted from the least altered lithology show significant differences of microstructure between matrix and the two rim layers (Fig. 10). The inter-chondrule matrix exhibits abundant crystalline fibrous silicates with large patches of TCI (Fig. 10b; Fig. 11a-b). The silicate groundmass for both the outer and inner rims is mostly amorphous or poorly crystallized fine-fibrous material and coarse-grained TCI are absent (Fig. 10c-d; Fig. 11 c-f). The outer rim (Fig. 10c; Fig. 11c-d) exhibits a high porosity compared to the matrix and the inner rim.

The matrix consists of an entanglement of domains of scarce amorphous silicates and phyllosilicates, as well as large patches of TCI (Fig. 11). Minor phases include coarse-grained tochilinite, anhydrous silicates (pyroxene and olivine), Fe-rich sulfides and organic matter. Nanosulfides are associated with amorphous silicates but are not present in phyllosilicates or TCIs (Fig. 11a). Their sizes range from 30 to 500 nm (average = 66 nm; N=132). The porosity (pore size ~ 200-400 nm) mostly surrounds the amorphous silicate domains. Fine-grained TCI surrounds coarse-grained tochilinite (Fig. 11b). Larger anhydrous silicates and sulfide grains (>200 nm) are also present. Phyllosilicates are chemically homogeneous with a serpentine composition. To assure the charge balance we found that Fe was distributed on the tetrahedral and octahedral sites with 13% and 87% respectively (assuming an equal distribution of Al on both site). We found the following structural formula $(Mg_{0.28}Al_{0.05}Fe_{0.67})_3(Si_{0.8}Al_{0.07}Fe_{0.13})_2O_5(OH)_4$ which is similar to previous composition measurements of serpentine in the same chondrite (Leroux et al., 2015).

The outer rim is dominated by amorphous silicate domains with embedded nanosulfides (Fig. 11c-d). Texturally, these domains are submicron-sized, irregularly molded and separated by pores often filled with carbon (either epoxy or indigenous organic matter). The domain size ranges from 300 nm to 1 µm with a mean value of 640 nm (N=60). The grain-size of nanosulfides ranges from 10 to 130 nm (average = 25 nm; N=683). The porosity is high (≈ 45 vol.%), in agreement with the SEM density measurements. Rare phyllosilicates (~ 50 nm large) occur around pyroxene grains (Fig. 11d).

The inner rim has a more compact texture with low porosity (~ 3 vol. %). Differences with SEM measurements are likely due to the size of the sample and to the lower precision of the ACADEMY method. In several locations the silicate is nanocrystalline. Two types of amorphous silicate domains occur and juxtapose each other. Some are sulfide-rich and some are sulfide-poor, as in the CM chondrite Yamato 791198 ((Chizmadia and Brearley, 2008); supplementary material 7). The nanosulfide grain size ranges from 30 to 250 nm with a mean size around 60 nm (N=126). Nanometer-wide Fe-rich veins appear to delimit sub-domains between the sulfide-poor amorphous silicate (green arrows; Fig. 11f). Domain sizes differ for the sulfide-poor and sulfide-rich region. They range from 140 nm to 700 nm for the sulfide-rich domains, and from 140 nm to 300 nm for the sulfide-poor domains. Mean domain sizes are 400 nm and 240 nm, respectively (N= 28 and 22). The sulfide-rich domains are associated with nanopores (mean pore-size ≈ 20 nm) while the sulfide-poor domains are less porous.

The contact between the chondrule and the inner rim (FIB 4) shows that the mesostasis glass is almost entirely *altered* to phyllosilicate and that the metal grain exhibits an oxidation rim (Fig. 12). Despite these alteration features, the adjacent inner rim appears to be more pristine and the contact between the chondrule and the rim is sharp. We did not find textural or chemical evolution in the inner rim as a function of the distance to the contact.

Quantitative chemistry and mineralogy using EDX mapping

Phase maps were obtained on the entire FIB sections (Fig. 13). Modal abundances are consistent with SEM data. The major component (>80%) of the matrix and FGRs is the silicate groundmass, which can now be resolved into amorphous silicate, mostly present in the rim, and phyllosilicate and TCI almost only found in the matrix (with varying proportions depending on the location). The groundmass contains anhydrous silicates and sulfides grains as seen at the SEM scale, but small grains of schreibersite, sulfate and chromite are now identified as well. Most of the anhydrous silicates are almost pure forsterite and enstatite. Few pyroxene grains enriched in Ca and Al have been identified in the three regions.

The modal abundance of nanosulfides associated with amorphous silicates are roughly identical for the three regions (6.5 to 10 ± 0.5 %). There are more grains in the outer rim but they are smaller, while the inner rim and the matrix display a population of larger grains that does not exist in the outer rim (Fig. 14). In comparison with matrix and with the inner rim, the outer rim displays a smooth distribution curve for sizes smaller than 50 nm with parameters a and b respectively larger and more negative for the exponential fitted curve (tail of the log-normal distribution).

The composition of the amorphous silicates is, to the first order, similar in the matrix, the inner and the outer rims (Fig 15). The average compositions are intermediate between saponite and serpentine stoichiometry. In the matrix, the amorphous silicates appear to be slightly enriched in Fe compared to the FGRs, possibly because nanometric TCI have not been filtered out. At the FIB section scale, the composition of the amorphous silicate is homogeneous. The pixel to pixel variability (within 1σ; pixel size=100 nm) of the amorphous silicate composition is higher in the matrix, with Fe/Mg ranging from 1 to 1.5 for the rim and 0.5 to 1.7 for the matrix, and with (Fe+Mg)/Si ranging from 1.2 to 1.4 in the rim and 1 to 1.8 in the matrix. S and Al concentrations are similar in the three regions, with S/Si ~ 0.2 and Al/Si ~0.1. Ca, Cr, Na and Ni have lower concentrations (X/Si<0.1). The small variability that exists is mostly due to mixing of nano-sulfides and TCI.

4. Discussion

4.1 A nebular, accretionary origin for the FGRs

A differential alteration for the FGRs and the adjacent matrix

FGRs in carbonaceous chondrites consist of an assemblage of phases that is often thought to be comparable to that of the matrix material (Metzler et al., 1992; Brearley, 1993; Zolensky et al., 1993; Hanowski and Brearley, 2000; Lauretta et al., 2000; Zega and Buseck, 2003; Chizmadia and Brearley, 2008). Nevertheless, investigating the least altered lithology of the Paris CM chondrite allowed us to reveal distinguishing features of FGRs and matrix.

Studied FGRs are mostly composed of amorphous silicate domains that embed small Fe-sulfide grains (<50 nm), organic compounds and anhydrous silicates (olivine and pyroxene). Amorphous silicates are known to be highly metastable (Rietmeijer et al., 2004; Chizmadia and Brearley, 2008; Nakamura-Messenger et al., 2011; Le Guillou and Brearley, 2014; Floss et al., 2014; Le Guillou et al., 2015a). When they interact with water, they rapidly transform into phyllosilicates, even at low temperature (Le Guillou et al., 2015b; Dobrica et al., 2019; Dobrică and Brearley, 2020). Hence, aqueous alteration was very limited in FGRs. The small size of the sulfides in the outer rim (<50 nm) is also indicative of limited alteration there. Sulfur has not been remobilized to form secondary phases typical of aqueous alteration (tochilinite and cronstedtite (Pignatelli et al., 2017). Porosity is higher in the outer rim, which is another indication of a limited alteration, because such an abundant porosity would have been the preferential location for precipitation of secondary phases. Compared to FGRs, matrix is more altered: the small anhydrous silicate grains are rarer, the sulfides are larger, and the porosity is lower. The secondary phases (phyllosilicates, TCI, carbonates and sulfates) are abundant and could have precipitated within the former porosity or replaced unstable phases (Zolensky et al., 1993; Rubin, 1997; Brearley, 2006; Howard et al., 2009; Howard et al., 2011; Le Guillou et al., 2015b; Pignatelli et al., 2017). Collectively, these characteristics indicate that the matrix and the FGRs of the Paris chondrite have undergone a differential alteration and that FGRs are more preserved than the matrix. These conclusions differ from some TEM studies of CM chondrites (Brearley, 1993; Zolensky et al., 1993; Lauretta et al., 2000; Zega and Buseck, 2003), likely because these previous studies were performed on chondrites more altered than Paris. Our observations are also in agreement with presolar grain abundances, which can be higher in rims than in the adjacent inter-chondrule matrices (Leitner et al., 2016).

To explain the differential alteration between matrix and rim, several scenarios can be discussed. Patches of amorphous silicates intermingled with phyllosilicates have the same composition in the matrix and the rims. This similar composition suggests that they originate from the same precursor, which underwent aqueous alteration in the matrix due to parent body processes. One possibility is that the matrix had been altered before it accreted with the rimmed chondrule, on a previous generation of parent body for instance. Another possibility is that part of the reservoir from which FGRs and matrix formed experienced higher temperature conditions leading to a – localized – lower amount of water which made preservation of the FGRs possible. Conversely, the matrix might have formed from the same reservoir from the point of view of silicates, but in a location where the amount of water was higher. The differential alteration between rims and matrix might hence be explained by this initial amount of water at the origin of distinct micro-chemical environments during parent body alteration. Previous studies already showed that aqueous alteration in Paris was not pervasive and water did not circulate at large

scale (Hewins et al., 2014; Leroux et al., 2015; Vacher et al., 2016; Pignatelli et al., 2017; Vinogradoff et al., 2017). Micro-chemical environments are favored for explaining the petrography of the matrix. The remaining pristine areas observed in the matrix in the present study is consistent with previous results. We suggest that the studied outer rims/inner rims and chondrules mostly escaped aqueous alteration due to the limited liquid water circulation. A part of the outer rim material (in the boundary) was however transformed (TCI formation) during the alteration of the matrix (Fig 3b). Within the more altered lithology, rims are more processed, TCI and carbonates patches are more abundant, suggesting that water circulate at larger scale (hundreds of micrometers).

Differential anhydrous silicate distribution in inner rim, outer rim and Matrix

Anhydrous silicates (olivine and pyroxenes) also reveal significant differences between the matrix and the FGRs. Firstly, a bimodal distribution is observed in the matrix whereas only one population, the smaller one (< 4μm), is present in FGRs. The coarse-grained population is probably the consequence of chondrule fragmentation (Grossman et al., 1988; Alexander et al., 1989). The small-grained population may have formed either by fragmentation as well – which should predate the event at the origin of the coarse-grained population, or by other mechanisms such as direct condensation of a nebular gas or crystallization due to thermal annealing of amorphous silicates (Palme and Fegley Jr, 1990; Brearley, 1993; Greshake, 1997). In any case, the shape (circularity, roundness solidity and aspect ratio; supplementary material 5) and chemical composition of these grains are similar for the matrix and the FGRs which indicate a similar origin. Secondly, the outer rim contains more of the smallest fraction of anhydrous silicates. This argues for the accretion of different ratios of anhydrous silicates and amorphous silicates. Finally, it should also be noted that the absence of the coarse-grained population in FGRs and the fact that FGRs never completely surround the chondrule fragments certainly indicate that chondrule fragmentation happened after the formation of FGRs.

Asteroidal vs. nebular environment for the FGR formation?

Two main scenarios have been proposed for the formation of FGRs: (1) FGRs formed by aqueous alteration either of the chondrule or the matrix in a parent-body (Sears et al., 1993; Tomeoka and Tanimura, 2000; Trigo-Rodriguez et al., 2006; Takayama and Tomeoka, 2012; Tomeoka and Ohnishi, 2014). (2) FGRs acquired their texture by accretion onto the chondrule (in the nebula) and were later altered to different degrees on the parent body (Brearley and Geiger, 1991; Metzler et al., 1992; Hanowski and Brearley, 2000; Hua et al., 2002; Zega and Buseck, 2003; Chizmadia and Brearley, 2008; Bland et al., 2011). The differential alteration between FGRs and matrix, as well as the differences in anhydrous silicate distribution and the FGR thickness/component radius relationship (Fig. 2, see Hanna and Ketcham, (2018)) argue against the first scenario. FGRs and especially outer rims are more porous but appear less altered than the matrix. If FGRs formed because of preferential circulation of fluids at the chondrule-matrix boundary, FGRs should be more altered than the matrix. This is the reverse of what we observe, in agreement with the abundances of presolar grains in FGRs of the most primitive chondrites (Leitner et al., 2016; Haenecour et al., 2018). This suggests that FGRs mostly escaped alteration. We conclude that an asteroidal alteration scenario is unlikely to explain the formation of FGRs and/or the differential alteration. We therefore suggest that FGRs formed by dust accretion onto the surface of chondrules, prior to their fragmentation and their integration into the matrix.

4.2 Inner rim accreted in hot conditions?

We argue that the outer rim is the material with the closest affinities to the dust precursor. This is supported by several lines of evidence: i) the outer rim shows almost no evidence of alteration or post-processing despite its high porosity; ii) it has the highest abundance of anhydrous silicates; iii) it has the smallest sulfide grain size. In contrast, the inner rim differs in several characteristics: i) it is less porous; ii) its abundance of anhydrous silicates is lower; iii) Nanometer-sized fibrous material occurs in the inner rim even if secondary phases such as phyllosilicates, carbonates or sulfates remain scarce; iiii) the inner rim contains sulfide-poor domains in addition to sulfide-rich domains and iiiii) the sulfide grain size is larger in the inner rim (80-100 nm vs. 30-50 nm in the outer rim). For these reasons, we suggest that the inner rim formed from a material that was initially like that of the outer rim but has been subsequently modified. In contrast to matrix material, we showed that aqueous alteration is unlikely to account for the characteristics of the inner rim, given the elevated abundance of amorphous silicate and the absence of secondary alteration phases. We suggest instead that a thermal event modified the inner rim in the nebula, during or after accretion to the chondrules. We present the following arguments in favor of this hypothesis.

Textural and chemical evolution of the layered rims of Paris

The porosity profile suggests that the inner rim was compacted before the outer rim was accreted (Fig. 8). Some studies proposed that rim compaction could occur during parent body lithification (Metzler et al., 1992; Chizmadia and Brearley, 2008; Tomeoka and Ohnishi, 2014; Hanna and Ketcham, 2018). Our observations are not consistent with this scenario because the full rim would have been compacted in a similar fashion, whereas there is a ~30 % porosity difference between the two rim layers. In addition, the preservation of high porosity in the outer rim shows that compaction was limited in the Paris parent body. The observed porosity profile in Paris FGRs suggests instead that rim compaction might have been thermally activated. Indeed, the evolution of the rim porosity profile in the least altered lithology of Paris shares similarities with experimental profiles obtained by accretion of dust onto a heated chondrule (1100°C) levitated in an inert gas (Beitz et al., 2013). In contrast, these authors have shown that at room temperature, the same experiment resulted in a flat porosity profile. Theoretical studies modelled the compaction of porous dust layers based on the physics of dust collisions (Morfill et al., 1998; Cuzzi, 2004; Ormel et al., 2008; Xiang et al., 2019). These studies showed that the accumulation and sticking of particles result in a radial porosity distribution, with the lowest value at the chondrule interface. As the dust accumulates, the compaction of the near-chondrule dust becomes more and more efficient while the outer part remains more porous. Based on the similarity of the porosity profiles between our observation, experiments and theoretical modelling, we suggest that the Paris chondrite has preserved the sequence of the radial evolution of dust accretion around chondrules and that the shape of the profile is partially due to the temperature effect.

Understanding the formation of the sulfide-rich and sulfide-poor amorphous domains in Paris is a key for deciphering why the inner rim and the outer rim are different. In the FGRs of Y-791198, (Chizmadia and Brearley, 2008) also observed sulfide-rich and sulfide-poor regions and suggested that it resulted from the accretion of dust with different thermal histories. According to this scenario, the inner rim of Paris would have also accreted dust from at least two sources, whereas the outer rim would have only sampled the sulfide-rich dust. Here we propose an alternative interpretation. If the source reservoir resembled the material found in the outer rim, heating this material might have generated the inner rim

characteristics. Indeed, sulfur would have been mobilized in the inner rim, forming larger sulfide grains and producing sulfide-poor areas. Thermal processing would have also favored viscous sintering of the amorphous material, resulting in a lower porosity and a higher compaction degree. The iron enrichment at the contacts between amorphous domains shows that iron has been mobilized along grain boundaries, possibly in relation to the remobilization of sulfides. Hence, thermal modification of the inner rim would altogether explain its low porosity compared to the outer rim, its grain sintering, as well as sulfide grain coarsening and sulfide poor/rich regions. In contrast, the outer rim and the matrix likely accreted later, in cooler conditions.

Formation scenarios of the inner rim

Several possibilities may account for the higher temperature that affected the inner rim in a nebular setting.

Scenario 1: Metzler et al. (1992) suggested that chondrules could have accreted a rim and formed a "primary rock". To explain the radial evolution of the rim of Paris, this early –inner – rim should have been compacted and thermally modified on a first parent body, then liberated and re-accreted with an additional layer of dust to form the pristine outer rim before being incorporated within the matrix to form a second parent body. Because the inner rim has been more thermally processed, the outer rim must have formed after the disruption of such "primary rock". If this scenario is correct, we would expect fragmented chondrules surrounded by a complete outer rim. However, outer rims only surround non-fragmented chondrules (Fig. 1).

Scenario 2: Warm nebular dust accreted onto chondrules is another possibility. After the chondrule formation, the surrounding dust might have experienced temperature excursion. This heated dust could accrete rapidly onto newly formed chondrules. In such a case, the chondrules and the dust have been hot enough to generate the inner rim characteristics. The outer rim and the matrix would have formed later, after the environment cooled down. This scenario is consistent with chondrule cooling rates. Chondrules isolated in vacuum would have cooled in a matter of seconds (Desch et al., 2012; Mann et al., 2016). However, textural, isotopic and experimental studies have shown that dust enrichment and evaporation in the chondrule formation region is a key for explaining many of the chondrule characteristics (Ebel and Grossman, 2000; Fedkin and Grossman, 2006; Alexander et al., 2008; Mathieu et al., 2011; Fedkin et al., 2012; Marrocchi and Chaussidon, 2015). This implies that the gas pressure was high enough to sustain heat for a longer time. Dust could therefore have been heated simultaneously, in the gas or while it was accreting onto warm chondrule. It is not excluded that a thermal gradient existed between the dust and the chondrule at the time they accreted together, as the cooling rates of these two materials are different.

Scenario 3: Chondrules might have accreted an early rim before being re-heated. Studies have shown that many chondrules experienced multiple heating events (e.g., Rubin and Krot, 1996). Igneous rims are sometimes observed and are interpreted as the melting of a dust-rich mantle accreted between two heating events (Rubin, 1984; Krot and Wasson, 1995; Rubin, 2010). In this scenario, the inner rims observed in the Paris chondrites would have been reheated, but to a moderate temperature. The outer rim and the matrix would be accreted after this heating episode in a colder environment.

Scenario 4: In high-speed collision conditions (KDA scenario), gas friction will heat the fast-moving objects. Inner rim thermal modification might also be a function of the initial speed of the object

entering a dusty gas region. As the chondrule (or other components) slowed down due to gas drag then the frictional heating effect also decreased. This model allows a qualitative understanding of how the inner FGR formed under warm conditions, while the outer FGR formed under cooler conditions.

To summarize, scenario 1 can be excluded, but 2, 3 and 4 are possible and not mutually exclusive.

Constraining the time-temperature of the inner rim formation

Several studies allow us to constrain the temperature range in which the inner rim could be modified. Davoisne et al. (2006) experimentally showed that a pure amorphous silicate thin film remains amorphous at a temperature up to 900 K, even for a long duration (~800 h). Conversely, other experimental studies have shown that in this range of temperature, sulfides could be easily mobilized (Grossman and Brearley, 2005; Abreu and Brearley, 2010; Palmer and Lauretta, 2011; Pignatelli et al., 2017) to form larger grains (i.e. grain coarsening). It should also be noted that the contacts between the amorphous domains, rich in FeO, and the crystalline silicates rich in Mg are chemically sharp. No Fe-Mg interdiffusion profile has been detected at the edge of the crystalline silicates. This shows that either the temperature did not reach high levels or that the heating episode was brief (Zolotov et al., 2006; Cuvillier et al., 2015). This absence of chemical exchange between silicates is of course compatible with the presence of abundant presolar grains in chondrule rims in C2 chondrites (Leitner et al., 2016; Haenecour et al., 2018). The preservation of the organic matter isotopic signature indicate that the temperature did not reach temperature greater than 500°C (Remusat et al., 2019). The Cr systematics for olivine also show that Type II chondrules were not significantly reheated (Hewins et al., 2014). The temperature must therefore have been high enough to mobilize the sulfur but low enough to avoid the Fe-Mg interdiffusion and preserve the amorphous silicates, the isotopic signature of the organic matter and the high abundance of presolar grains.

These elements allow us to discuss the different scenario: (1) Scenario 1 is unlikely to produce a brief heating episode. (2) In the scenario 2, in view of the estimated temperatures, the chondrule cooling rates imply that inner rim accretion occurred rapidly after chondrule formation. Indeed, between the silicate liquidus and solidus, cooling rates varies between 10-1000 K/hr (1700-2000 K) and 1-1000 K/hr (1000-1600K) (Radomsky and Hewins, 1990; Yu and Hewins, 1998; Harker and Desch, 2002; Hewins et al., 2005; Berlin et al., 2011; Desch et al., 2012; Perez et al., 2018). It could be even faster in the subsolidus according to other authors (Villeneuve et al., 2015; Marrocchi et al., 2019). At lower temperature, relevant to the inner rim formation, cooling rates are even more poorly constrained. A recent study based on sulfide composition proposed rates of 10 - 100 K/hr for temperature <900 K (Schrader et al., 2018). Despite these difficulties in constraining chondrule cooling rates, all estimates imply that inner rim accretion could have happened within a range of a few hours (i.e., ~1-100 h). (3) Cooling rates for a particle interacting at high speed with a dust-rich environment have already been studied and are relevant for the scenario 4. For instance, Liffman and Toscano (2000), in their Figure 2, showed that particles heated to a temperature range between 500 K and 1000 K cool at rates between 10 K/hour and 100 K/hour which is also consistent with an inner rim accretion in a few hours (i.e., ~1-100 h).

4.3 Assembling and transforming the Paris parent body

We propose the following steps for the formation of the Paris chondrite parent body (Fig. 16) :

(1) FGRs were accreted in a nebular, dust-rich environment. In this environment, thermal modification of the dust occurred (silicate sintering, sulfur redistribution and compaction) which led to the inner rim characteristic. Potential heat sources are contact with a warm chondrule, thermal radiation before accretion, multiple heating or high-speed collision/friction. In these conditions, the amount of water the dust was certainly low.

(2) The outer rim was accreted afterward in a colder environment. The limited aqueous alteration of the inner and outer rim indicates that the amount of water in the rim was low after accretion onto chondrules. This suggest that even though the outer rim accreted in colder conditions, they were still warm enough to dry the accreted dust. The abundance of sub-micrometric anhydrous silicates was higher during the outer rim accretion.

(3) After FGR accretion on chondrules, chondrule fragments were produced, likely by collisions. These fragments constitute the large anhydrous grains population observed in the matrix. Rimmed chondrules, fragmented chondrules and remaining dust were accreted to form the Paris parent body in a colder environment with a higher amount of water.

(4) In the least altered area, aqueous alteration of the matrix occurred leading to the formation of TCI patches and phyllosilicates. The alteration affected similarly the “chondrule/inner rim/outer rim” assemblage to a lower degree. The inner rim however exhibits the features of thermal modifications in the nebula. In the more altered regions, alteration occurred on a larger scale and homogenized rims and matrix (Fig 3 and supplementary material 8). A brecciation process involving rocks originating from different depths of the parent body could explain the association between these two lithologies (Marrocchi et al., 2014; Hewins et al., 2014; Pignatelli et al., 2017; Vinogradoff et al., 2017).

5. Conclusion

This multi-scale quantitative study of fine-grained material in the Paris chondrite revealed significant differences between the matrix and fine-grained rims around chondrules, offering a new insight into the processing of the dust in the protoplanetary disk. The matrix and FGR precursor materials originate from the same reservoir. However, the matrix shows more advanced alteration, suggesting that the amount of water was higher at the time of its accretion compared to that of the FGRs. The FGR material was certainly heated at mild-moderate temperature, leading to drier conditions. The matrix accreted later, in a colder environment and thus richer in water, together with chondrule fragments and rimmed chondrules to form the Paris parent body.

The study of other slightly altered chondrites should allow us to better constrain these thermal, spatial and temporal environments. The statistical study of the different types of chondrules is also fundamental since their cooling rates may differ. If the FGRs are effectively related to the formation and cooling of chondrules, we expect to find different degrees of transformation of the FGRs in different types of chondrites/chondrules. Finally, these further studies could offer us new insights on the physics of the first stages of accretion of the chondrite's components and on the formation of the first parent bodies in the early solar system.

Acknowledgements:

We thank Hope Ishii and two anonymous reviewers that provided constructive reviews that significantly improved the manuscript. This work was supported by the Programme National de Planétologie (PNP) of CNRS/INSU, co-funded by CNES. The SEM and EPMA works were done at the electron microscope facility at the University of Lille with the support of the Chevreul Institute, the European FEDER and Région Hauts-de-France. We thank the Muséum National d'Histoire Naturelle (Paris) for providing the section of the Paris chondrite. We thank David Troadec for the high-quality FIB sections, partly supported by the French RENATECH network. We also thank the Department of Mineral Sciences of the Smithsonian institution for providing us with microbeam reference standards (catalog number: 117733-85276-111356-115900-114887-R2460). We thank the SARM (Service d'Analyse des Roches et des Minéraux) for providing us the Biotite. PM Zanetta thanks Ahmed Addad, Maya Marinova and Séverine Bellayer for their assistance with the electron microscope instruments.

References

Abreu N. M. and Brearley A. J. (**2010**) Early solar system processes recorded in the matrices of two highly pristine CR3 carbonaceous chondrites, MET 00426 and QUE 99177. *Geochim. Cosmochim. Acta* **74**, 1146–1171. Available at: http://www.sciencedirect.com/science/article/pii/S001670370900708X.

Alexander C. M. O., Hutchison R. and Barber D. J. (**1989**) Origin of chondrule rims and interchondrule matrices in unequilibrated ordinary chondrites. *Earth Planet. Sci. Lett.* **95**, 187–207.

Alexander C. M. O. D., Grossman J. N., Ebel D. S. and Ciesla F. J. (**2008**) The formation conditions of chondrules and chondrites. *Science (80-.).* **320**, 1617–1619.

Barrat J.-A., Zanda B., Moynier F., Bollinger C., Liorzou C. and Bayon G. (**2012**) Geochemistry of CI chondrites: Major and trace elements, and Cu and Zn isotopes. *Geochim. Cosmochim. Acta* **83**, 79–92.

Beitz E., Blum J., Mathieu R., Pack A. and Hezel D. C. (**2013**) Experimental investigation of the nebular formation of chondrule rims and the formation of chondrite parent bodies. *Geochim. Cosmochim. Acta* **116**, 41–51.

Berlin J., Jones R. H. and Brearley A. J. (**2011**) Fe-Mn systematics of type IIA chondrules in unequilibrated CO, CR, and ordinary chondrites. *Meteorit. Planet. Sci.* **46**, 513–533.

Bland P. A., Howard L. E., Prior D. J., Wheeler J., Hough R. M. and Dyl K. A. (**2011**) Earliest rock fabric formed in the Solar System preserved in a chondrule rim. *Nat. Geosci.* **4**, 244.

Brearley A. J. and Geiger T. (**1991**) Mineralogical and chemical studies bearing on the origin of accretionary rims in the Murchison CM2 carbonaceous chondrite. *Meteoritics* **26**, 323.

Brearley A. J. (**1993**) Matrix and fine-grained rims in the unequilibrated CO3 chondrite, ALHA77307: Origins and evidence for diverse, primitive nebular dust components. *Geochim. Cosmochim. Acta* **57**, 1521–1550.

Brearley A. J. (**2006**) The Action of Water. *Meteorites Early Sol. Syst. II*, 584–624.

Chizmadia L. J. and Brearley A. J. (**2008**) Mineralogy, aqueous alteration, and primitive textural characteristics of fine-grained rims in the Y-791198 {CM}2 carbonaceous chondrite: {TEM} observations and comparison to {ALHA}81002. *Geochim. Cosmochim. Acta* **72**, 602–625.

Cuvillier P., Leroux H., Jacob D. and Hirel P. (**2015**) Fe-Mg interdiffusion profiles in rimmed forsterite grains in the Allende matrix: time--temperature constraints for the parent body metamorphism. *Meteorit. Planet. Sci.* **50**, 1529–1545.

Cuzzi J. N. (**2004**) Blowing in the wind: III. Accretion of dust rims by chondrule-sized particles in a turbulent protoplanetary nebula. *Icarus* **168**, 484–497.

Davoisne C., Djouadi Z., Leroux H., d'Hendecourt L., Jones A. and Deboffle D. (**2006**) The origin of GEMS in IDPs as deduced from microstructural evolution of amorphous silicates with annealing. *Astron. Astrophys.* **448**, L1--L4.

Desch S. J., Morris M. A., Connolly Jr H. C. and Boss A. P. (**2012**) The importance of experiments: Constraints on chondrule formation models. *Meteorit. Planet. Sci.* **47**, 1139–1156.

Dobrica E., Guillou C. Le and Brearley A. J. (**2019**) Aqueous alteration of porous microchondrules in

Semarkona: Implications for hydration, oxidation and elemental exchange processes. *Geochim. Cosmochim. Acta* **244**, 292–307. Available at: http://www.sciencedirect.com/science/article/pii/S0016703718305763.

Dobrică E. and Brearley A. J. (**2020**) Amorphous silicates in the matrix of Semarkona: The first evidence for the localized preservation of pristine matrix materials in the most unequilibrated ordinary chondrites. *Meteorit. Planet. Sci.*, maps.13458. Available at: https://onlinelibrary.wiley.com/doi/abs/10.1111/maps.13458 [Accessed April 8, 2020].

Ebel D. S. and Grossman L. (**2000**) Condensation in dust-enriched systems. *Geochim. Cosmochim. Acta* **64**, 339–366.

Fedkin A. V and Grossman L. (**2006**) The fayalite content of chondritic olivine: Obstacle to understanding the condensation of rocky material. *Meteorites early Sol. Syst. II*, 279–294.

Fedkin A. V, Grossman L., Ciesla F. J. and Simon S. B. (**2012**) Mineralogical and isotopic constraints on chondrule formation from shock wave thermal histories. *Geochim. Cosmochim. Acta* **87**, 81–116.

Ferreira T. and Rasb W. (**2012**) ImageJ User Guide. Available at: http://citeseerx.ist.psu.edu/viewdoc/summary?doi=10.1.1.465.6195 [Accessed October 12, 2020].

Floss C., Le Guillou C. and Brearley A. (**2014**) Coordinated NanoSIMS and FIB-TEM analyses of organic matter and associated matrix materials in CR3 chondrites. *Geochim. Cosmochim. Acta* **139**, 1–25.

Gonzalez J.-F., Laibe G., Maddison S. T., Pinte C. and Ménard F. (**2015**) The accumulation and trapping of grains at planet gaps: effects of grain growth and fragmentation. *Planet. Space Sci.* **116**, 48–56.

Gonzalez J. F., Laibe G. and Maddison S. T. (**2017**) Self-induced dust traps: Overcoming planet formation barriers. *Mon. Not. R. Astron. Soc.* **467**, 1984–1996.

Greshake A. (**1997**) The primitive matrix components of the unique carbonaceous chondrite Acfer 094: A {TEM} study. *Geochim. Cosmochim. Acta* **61**, 437–452.

Grossman J. N., Rubin A. E., Nagahara H. and King E. A. (**1988**) Properties of chondrules. *Meteorites early Sol. Syst.*, 619–659.

Grossman J. N. and Brearley A. J. (**2005**) The onset of metamorphism in ordinary and carbonaceous chondrites. *Meteorit. Planet. Sci.* **40**, 87–122.

Le Guillou C. and Brearley A. (**2014**) Relationships between organics, water and early stages of aqueous alteration in the pristine {CR}3.0 chondrite {MET} 00426. *Geochim. Cosmochim. Acta* **131**, 344–367.

Le Guillou C., Changela G. H. and Brearley A. J. (**2015a**) Widespread oxidized and hydrated amorphous silicates in CR chondrites matrices: Implications for alteration conditions and H2 degassing of asteroids. *Earth Planet. Sci. Lett.* **420**, 162–173. Available at: http://www.sciencedirect.com/science/article/pii/S0012821X1500117X.

Le Guillou C., Dohmen R., Rogalla D., Müller T., Vollmer C. and Becker H. W. (**2015b**) New experimental approach to study aqueous alteration of amorphous silicates at low reaction rates. *Chem. Geol.* **412**, 179–192.

Le Guillou C., Leroux H., Zanetta P. M., Brearley A. J., De La Pena F. and Marinova M. (**2018**) Water Content in Amorphous Silicates of Chondrite Matrices Determined by Advanced TEM Analysis---And Scanning Transmission X-Ray Microscopy. In *Lunar and Planetary Science Conference*

Haenecour P., Floss C., Zega T. J., Croat T. K., Wang A., Jolliff B. L. and Carpenter P. (**2018**) Presolar silicates in the matrix and fine-grained rims around chondrules in primitive CO3. 0 chondrites: Evidence for pre-accretionary aqueous alteration of the rims in the solar nebula. *Geochim. Cosmochim. Acta* **221**, 379–405.

Hanna R. D. and Ketcham R. A. (**2018**) Evidence for accretion of fine-grained rims in a turbulent nebula for {CM} Murchison. *Earth Planet. Sci. Lett.* **481**, 201–211.

Hanowski N. P. and Brearley A. J. (**2000**) Iron-rich aureoles in the CM carbonaceous chondrites Murray, Murchison, and Allan Hills 81002: Evidence for in situ aqueous alteration. *Meteorit. Planet. Sci.* **35**, 1291–1308.

Hanowski N. P. and Brearley A. J. (**2001**) Aqueous alteration of chondrules in the CM carbonaceous chondrite, Allan Hills 81002: implications for parent body alteration. *Geochim. Cosmochim. Acta* **65**, 495–518. Available at: http://www.sciencedirect.com/science/article/pii/S0016703700005524.

Harker D. E. and Desch S. J. (**2002**) Annealing of silicate dust by nebular shocks at 10 AU. *Astrophys. J. Lett.* **565**, L109.

Hewins R. H., Connolly H. C., Lofgren Jr G. E. and Libourel G. (**2005**) Experimental constraints on chondrule formation. In *Chondrites and the protoplanetary disk* p. 286.

Hewins R. H., Bourot-Denise M., Zanda B., Leroux H., Barrat J.-A., Humayun M., Göpel C., Greenwood R. C., Franchi I. A., Pont S. and others (**2014**) The Paris meteorite, the least altered CM chondrite so far. *Geochim. Cosmochim. Acta* **124**, 190–222.

Howard K. T., Benedix G. K., Bland P. A. and Cressey G. (**2009**) Modal mineralogy of CM2 chondrites by X-ray diffraction (PSD-XRD). Part 1: Total phyllosilicate abundance and the degree of aqueous alteration. *Geochim. Cosmochim. Acta* **73**, 4576–4589.

Howard K. T., Benedix G. K., Bland P. A. and Cressey G. (**2011**) Modal mineralogy of CM chondrites by X-ray diffraction (PSD-XRD): Part 2. Degree, nature and settings of aqueous alteration. *Geochim. Cosmochim. Acta* **75**, 2735–2751.

Hua X., Wang J. and BUSECK P. R. (**2002**) Fine-grained rims in the Allan Hills 81002 and Lewis Cliff 90500 CM2 meteorites: Their origin and modification. *Meteorit. Planet. Sci.* **37**, 229–244.

Johansen A., Mac Low M.-M., Lacerda P. and Bizzarro M. (**2015a**) Growth of asteroids, planetary embryos, and Kuiper belt objects by chondrule accretion. *Sci. Adv.* **1**, e1500109.

Johansen A., Jacquet E., Cuzzi J. N., Morbidelli A. and Gounelle M. (**2015b**) New paradigms for asteroid formation. *Asteroids IV*, 471–491.

Krot A. N. and Wasson J. T. (**1995**) Igneous rims on low-FeO and high-FeO chondrules in ordinary chondrites. *Geochim. Cosmochim. Acta* **59**, 4951–4966.

de la Peña F., Prestat E., Fauske V. T., Burdet P., Jokubauskas P., Nord M., Ostasevicius T., MacArthur K. E., Sarahan M., Johnstone D. N., Taillon J., Lähnemann J., Migunov V., Eljarrat A., Caron J., Aarholt T., Mazzucco S., Walls M., Slater T., Winkler F., pquinn-dls, Martineau B., Donval G., McLeod R., Hoglund E. R., Alxneit I., Lundeby D., Henninen T., Zagonel L. F. and Garmannslund A. (**2019**) hyperspy/hyperspy: HyperSpy v1.5.2. Available at: https://doi.org/10.5281/zenodo.3396791.

Laibe G., Gonzalez J.-F., Fouchet L. and Maddison S. T. (**2008**) SPH simulations of grain growth in protoplanetary disks. *Astron. Astrophys.* **487**, 265–270.

Lanari P., Vidal O., De Andrade V., Dubacq B., Lewin E., Grosch E. G. and Schwartz S. (**2014**) XMapTools: A MATLAB{\copyright}-based program for electron microprobe X-ray image processing and geothermobarometry. *Comput. Geosci.* **62**, 227–240.

Lauretta D. S., Hua X. and Buseck P. R. (**2000**) Mineralogy of fine-grained rims in the ALH 81002 CM chondrite. *Geochim. Cosmochim. Acta* **64**, 3263–3273.

Leitner J., Vollmer C., Floss C., Zipfel J. and Hoppe P. (**2016**) Ancient stardust in fine-grained chondrule dust rims from carbonaceous chondrites. *Earth Planet. Sci. Lett.* **434**, 117–128. Available at: http://dx.doi.org/10.1016/j.epsl.2015.11.028.

Leroux H., Cuvillier P., Zanda B. and Hewins R. H. (**2015**) GEMS-like material in the matrix of the Paris meteorite and the early stages of alteration of CM chondrites. *Geochim. Cosmochim. Acta* **170**, 247–265.

Liffman K. (**2000**) Chondrule Fine-Grained Mantle Formation by Hypervelocity Impact of Chondrules with a Dusty Gas. *Icarus* **143**, 106–125.

Liffman K. (**2019**) Fine-grained rim formation - high speed, kinetic dust aggregation in the early Solar System. *Geochim. Cosmochim. Acta*. Available at: http://www.sciencedirect.com/science/article/pii/S0016703719305071.

Lodders K. and Palme H. (**2009**) Solar system elemental abundances in 2009. *Meteorit. Planet. Sci. Suppl.* **72**, 5154.

Mann C. R., Boley A. C. and Morris M. A. (**2016**) Planetary embryo bow shocks as a mechanism for chondrule formation. *Astrophys. J.* **818**, 103.

Marrocchi Y., Gounelle M., Blanchard I., Caste F. and Kearsley A. T. (**2014**) The Paris CM chondrite: Secondary minerals and asteroidal processing. *Meteorit. Planet. Sci.* **49**, 1232–1249.

Marrocchi Y. and Chaussidon M. (**2015**) A systematic for oxygen isotopic variation in meteoritic chondrules. *Earth Planet. Sci. Lett.* **430**, 308–315.

Marrocchi Y., Villeneuve J., Jacquet E., Piralla M. and Chaussidon M. (**2019**) Rapid condensation of the first Solar System solids. *Proc. Natl. Acad. Sci.* **116**, 23461–23466. Available at: https://www.pnas.org/content/116/47/23461 [Accessed June 2, 2020].

Mathieu R., Libourel G., Deloule E., Tissandier L., Rapin C. and Podor R. (**2011**) Na2O solubility in CaO--MgO--SiO2 melts. *Geochim. Cosmochim. Acta* **75**, 608–628.

Metzler K., Bischoff A. and Stöffler D. (**1992**) Accretionary dust mantles in CM chondrites: Evidence for solar nebula processes. *Geochim. Cosmochim. Acta* **56**, 2873–2897.

Morbidelli A., Lunine J. I., O'Brien D. P., Raymond S. N. and Walsh K. J. (**2012**) Building terrestrial planets. *Annu. Rev. Earth Planet. Sci.* **40**, 251–275.

Morfill G. E., Durisen R. H. and Turner G. W. (**1998**) An Accretion Rim Constraint on Chondrule Formation Theories. *Icarus* **134**, 180–184.

Nakamura-Messenger K., Clemett S. J., Messenger S. and Keller L. P. (**2011**) Experimental aqueous alteration of cometary dust. *Meteorit. Planet. Sci.* **46**, 843–856.

Ormel C. W., Cuzzi J. N. and Tielens A. (**2008**) Co-accretion of chondrules and dust in the solar nebula.

Astrophys. J. **679**, 1588.

Palme H. and Fegley Jr B. (**1990**) High-temperature condensation of iron-rich olivine in the solar nebula. *Earth Planet. Sci. Lett.* **101**, 180–195.

Palmer E. E. and Lauretta D. S. (**2011**) Aqueous alteration of kamacite in CM chondrites. *Meteorit. Planet. Sci.* **46**, 1587–1607.

Perez A. M., Desch S. J., Schrader D. L. and Till C. B. (**2018**) An Experimental Investigation of the Planetary Embryo Bow Shock Model as a Chondrule Formation Mechanism. In *Lunar and Planetary Science Conference*

Piani L., Yurimoto H. and Remusat L. (**2018**) A dual origin for water in carbonaceous asteroids revealed by CM chondrites. *Nat. Astron.* **2**, 317–323. Available at: https://doi.org/10.1038/s41550-018-0413-4.

Pignatale F. C., Charnoz S., Chaussidon M. and Jacquet E. (**2018**) Making the Planetary Material Diversity during the Early Assembling of the Solar System. *Astrophys. J. Lett.* **867**, L23.

Pignatelli I., Marrocchi Y., Mugnaioli E., Bourdelle F. and Gounelle M. (**2017**) Mineralogical, crystallographic and redox features of the earliest stages of fluid alteration in {CM} chondrites. *Geochim. Cosmochim. Acta* **209**, 106–122.

Radomsky P. M. and Hewins R. H. (**1990**) Formation conditions of pyroxene-olivine and magnesian olivine chondrules. *Geochim. Cosmochim. Acta* **54**, 3475–3490.

Remusat L., Bonnet J. Y., Bernard S., Buch A. and Quirico E. (**2019**) Molecular and isotopic behavior of insoluble organic matter of the Orgueil meteorite upon heating. *Geochim. Cosmochim. Acta* **263**, 235–247.

Rietmeijer F. J. M., Nuth III J. A. and Nelson R. N. (**2004**) Laboratory hydration of condensed magnesiosilica smokes with implications for hydrated silicates in IDPs and comets. *Meteorit. Planet. Sci.* **39**, 723–746.

Rubin A. E. (**1984**) Coarse-grained chondrule rims in type 3 chondrites. *Geochim. Cosmochim. Acta* **48**, 1779–1789.

Rubin A. E. and Krot A. N. (**1996**) Multiple heating of chondrules. *cpd*, 173–180.

Rubin A. E. (**1997**) Mineralogy of meteorite groups. *Meteorit. Planet. Sci.* **32**, 231–247.

Rubin A. E. (**2010**) Physical properties of chondrules in different chondrite groups: Implications for multiple melting events in dusty environments. *Geochim. Cosmochim. Acta* **74**, 4807–4828.

Schrader D. L., Fu R. R., Desch S. J. and Davidson J. (**2018**) The background temperature of the protoplanetary disk within the first four million years of the Solar System. *Earth Planet. Sci. Lett.* **504**, 30–37. Available at: http://www.sciencedirect.com/science/article/pii/S0012821X18305697.

Sears D. W. G., Benoit P. H. and Jie L. (**1993**) Two chondrule groups each with distinctive rims in Murchison recognized by cathodoluminescence. *Meteoritics* **28**, 669–675.

Takayama A. and Tomeoka K. (**2012**) Fine-grained rims surrounding chondrules in the Tagish Lake carbonaceous chondrite: Verification of their formation through parent-body processes. *Geochim. Cosmochim. Acta* **98**, 1–18. Available at: http://dx.doi.org/10.1016/j.gca.2012.08.015.

Tomeoka K. and Tanimura I. (**2000**) Phyllosilicate-rich chondrule rims in the vigarano cv3 chondrite:

780 evidence for parent-body processes. *Geochim. Cosmochim. Acta* **64**, 1971–1988.

781 **Tomeoka K. and Ohnishi I.** (**2014**) Olivine-rich rims surrounding chondrules in the Mokoia CV3
782 carbonaceous chondrite: Further evidence for parent-body processes. *Geochim. Cosmochim. Acta*
783 **137**, 18–34.

784 **Trigo-Rodriguez J. M., Rubin A. E. and Wasson J. T.** (**2006**) Non-nebular origin of dark mantles around
785 chondrules and inclusions in CM chondrites. *Geochim. Cosmochim. Acta* **70**, 1271–1290.

786 **Villeneuve J., Libourel G. and Soulié C.** (**2015**) Relationships between type I and type II chondrules:
787 Implications on chondrule formation processes. *Geochim. Cosmochim. Acta* **160**, 277–305.

788 **Vinogradoff V., Guillou C. Le, Bernard S., Binet L., Cartigny P., Brearley A. J. and Remusat L.** (**2017**) Paris
789 vs. Murchison: Impact of hydrothermal alteration on organic matter in {CM} chondrites. *Geochim.*
790 *Cosmochim. Acta* **212**, 234–252.

791 **Watanabe M. and Williams D. B.** (**2006**) The quantitative analysis of thin specimens: a review of progress
792 from the Cliff-Lorimer to the new $ζ$-factor methods. *J. Microsc.* **221**, 89–109.

793 **Xiang C., Carballido A., Hanna R. D., Matthews L. S. and Hyde T. W.** (**2019**) The initial structure of
794 chondrule dust rims I: Electrically neutral grains. *Icarus* **321**, 99–111.

795 **Yu Y. and Hewins R. H.** (**1998**) Transient heating and chondrule formation: Evidence from sodium loss in
796 flash heating simulation experiments. *Geochim. Cosmochim. Acta* **62**, 159–172.

797 **Zanetta P.-M., Le Guillou C., Leroux H., Zanda B., Hewins R. H., Lewin E. and Pont S.** (**2019**) Modal
798 abundance, density and chemistry of micrometer-sized assemblages by advanced electron
799 microscopy: Application to chondrites. *Chem. Geol.* **514**, 27–41. Available at:
800 https://doi.org/10.1016/j.chemgeo.2019.03.025.

801 **Zega T. J. and Buseck P. R.** (**2003**) Fine-grained-rim mineralogy of the Cold Bokkeveld CM chondrite.
802 *Geochim. Cosmochim. Acta* **67**, 1711–1721.

803 **Zolensky M., Barrett R. and Browning L.** (**1993**) Mineralogy and composition of matrix and chondrule rims
804 in carbonaceous chondrites. *Geochim. Cosmochim. Acta* **57**, 3123–3148.

805 **Zolotov M. Y., Mironenko M. V and Shock E. L.** (**2006**) Thermodynamic constraints on fayalite formation
806 on parent bodies of chondrites. *Meteorit. Planet. Sci.* **41**, 1775–1796.

807

808

Appendix

1. Statistical analysis based on BSE montage.

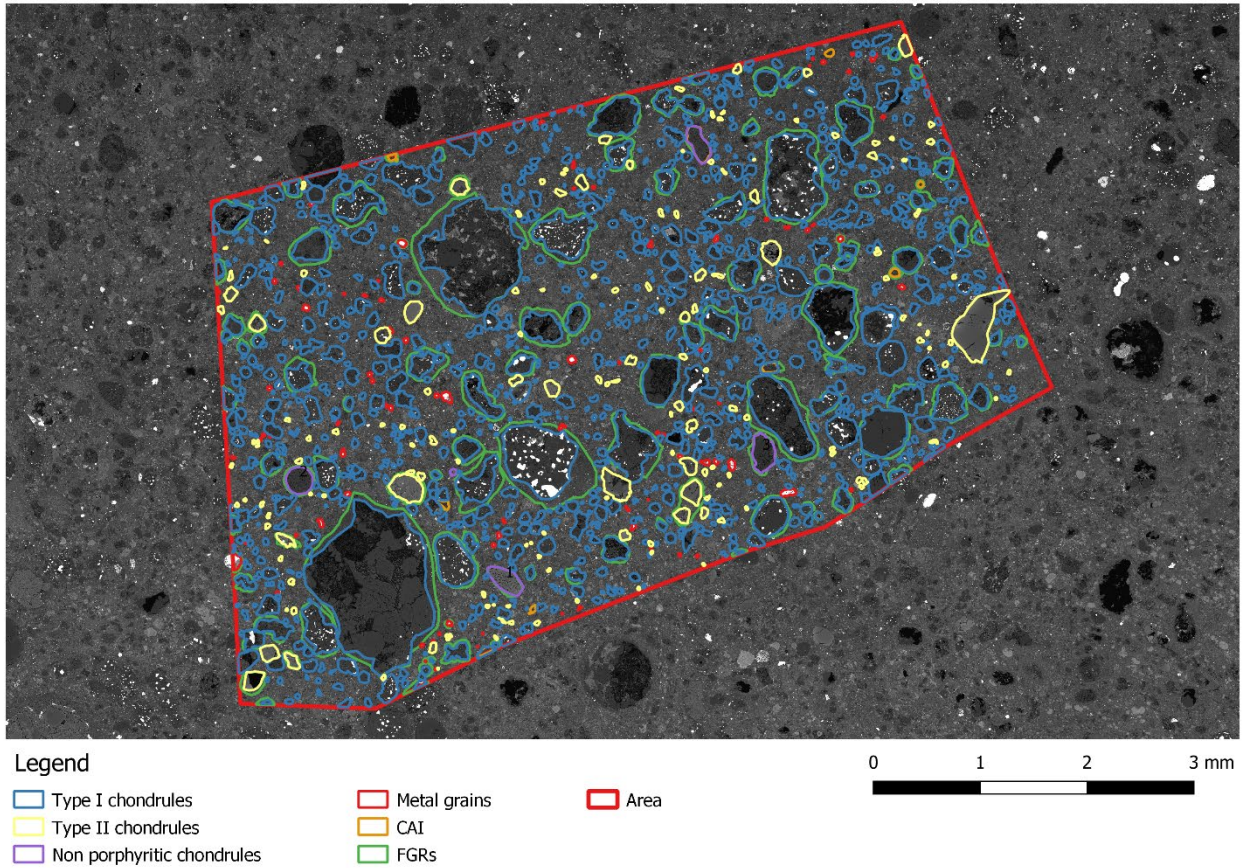

This figure represents the 33 mm² area analyzed with Qgis® software. The resolution of the map is 1µm / pixel. The different types of chondrules are distinguished. The abundance of chondrules, their types, and the thickness of their rims could be analyzed using this software (see table below).

	All components						
	Component parameters				FGR parameters		
	Area (%)	Number	Mean Radius (µm)	Rimmed fraction (%)	Area (%)	Number	Mean Thickness rim (µm)
Type 1 chondrules	30.44	939	38.8	9.4	5.9	88	21.5
Type 2 chondrules	2.44	158	28.5	10.8	0.3	17	14.4
Non porphyritic chondrules	0.66	6	105.6	33.3	0.1	2	10.3
Metal grains	0.34	89	17.2	13.5	0.0	12	10.3
CAIs	0.27	10	45.2	80.0	0.1	8	8.7
Total	**34.15**	**1202**			6.4	127	

Table : Abundances and parameters of high temperature components and of FGRs deduced from BSE image (30 mm^2) analysis using QGis®, in the least altered region of Paris.

2. Phase abundance in the different areas (SEM).

		Map 1			Map 2			Map 3			Map 4		
		Inner Rim	Outer Rim	Matrix	Inner Rim	Outer Rim	Matrix	Inner Rim	Outer Rim	Matrix	Inner Rim	Outer Rim	Matrix
Inclusions	Metal grain		0,00	0,72	0,00	0,05	0,03	0,00		0,01			
	Oxides	0,09	0,01	0,29									
	Olivine	1,32	2,98	3,82	1,35	2,75	2,67	0,97	1,68	7,04	0,64	0,52	0,55
	Enstatite	0,76	1,28	2,28	1,34	2,31	5,04	0,56	0,70	1,64	2,62	3,44	6,32
	Ca-pyroxene				0,23	0,82	0,81	0,85	0,84	0,99			
	Fe-rich sulfides	0,07	0,33	0,43	0,32	0,79	0,29	0,09	0,28	0,97	0,21	0,20	0,63
	Pentlandite	0,08	0,13	0,43	0,22	0,45	0,36	0,20	0,10	0,35	0,06	0,02	0,80
	Carbonates	0,02	0,03	0,28	0,00	0,02	0,99	0,04	0,46	1,01	0,01	0,01	1,55
	Sulfates	0,01	0,34	1,47	0,07	0,30	1,82	0,08	0,51	0,74	0,06	0,09	2,60
Surrounding material	TCI-T	0,37	0,71	4,54	2,58	4,66	12,36	1,21	2,64	3,88			
	TCI-C	1,16	0,36	6,44	15,34	12,01	19,36	13,56	16,55	30,25	1,76	12,23	6,71
	Fe-rich Phyll/amorph	81,63	54,48	57,01	78,52	75,68	54,69	82,45	76,23	53,11	25,12	29,26	26,83
	Mg-rich Phyll/amorph	14,40	39,27	21,85							69,34	53,56	53,31
	Al-rich Phyll/amorph				0,02	0,03	0,53						
Other phases	Apatite					0,12	0,98				0,19	0,65	0,71
	Alumina corundum				0,00	0,01	0,05						
	Spinel					0,00	0,02						
	Mesostasis	0,10	0,06	0,44									
	Total	100,00	100,00	100,00	100,00	100,00	100,00	100,00	100,00	100,00	100,00	100,00	100,00

Table: Modal abundances are extracted from the different SEM phase maps using the ACADEMY methodology from (Zanetta et al., 2019). In map 2 the two rims are averaged. Map 4 is taken in the more altered lithology of Paris.

3. Composition fields

In this part we show the composition fields and the different clusters associated with the fine and interstitial material present in the Paris matrix. In comparison with the amorphous silicate groundmass and phyllosilicates, TCIs are easily distinguished (plot b).

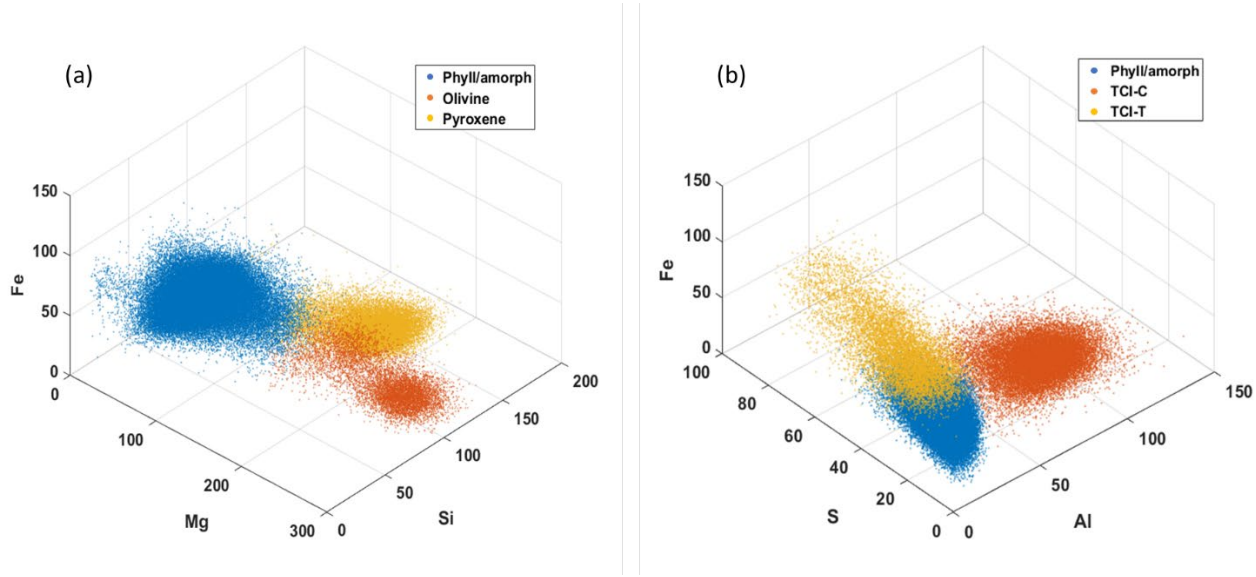

(a) Fe, Mg and Si plot 3D for the amorphous groundmass (+ phyllosilicates), olivine and pyroxene. (b) Fe, S and Al plot 3D for the amorphous groundmass (+ phyllosilicates), TCI-C and TCI-T.

4. Mask for the counting of the larger grains

We present the mask used for the size distribution of anhydrous silicates in Paris meteorite. Chondrules and chondrule fragments (Mg endmember) are well identified on this image and were used to plot the bimodal distribution shown in Fig. 6.

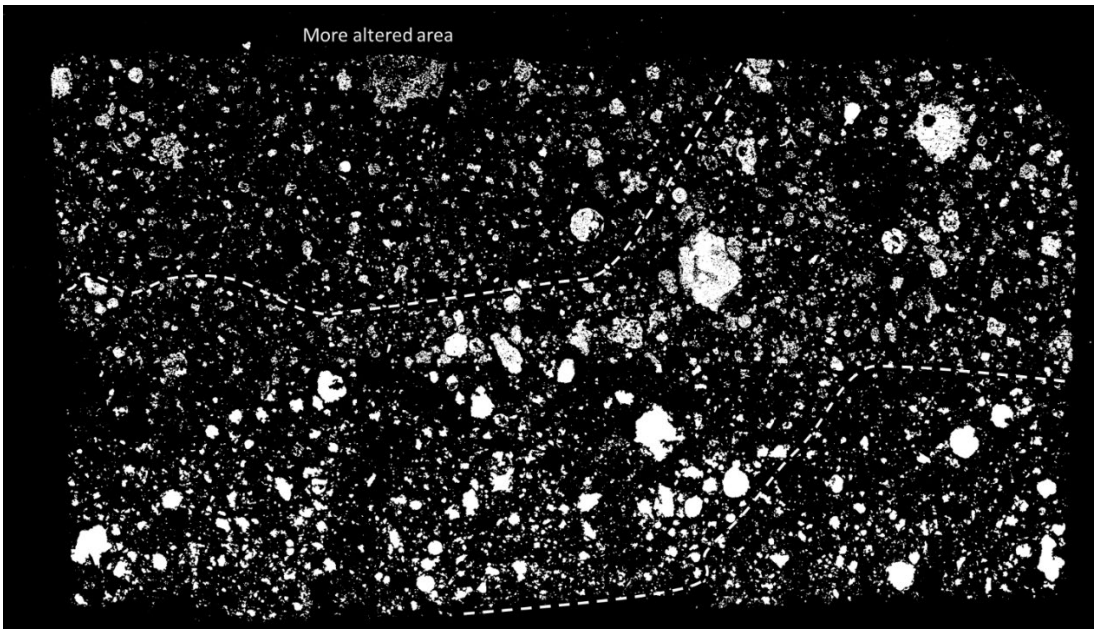

Thresholded and denoised BSE mosaic. The resolution of the map is 1µm / pixel. The mask was created by thresholding on the gray levels. Isolated pixels (1µm) were considered as noise and were deleted.

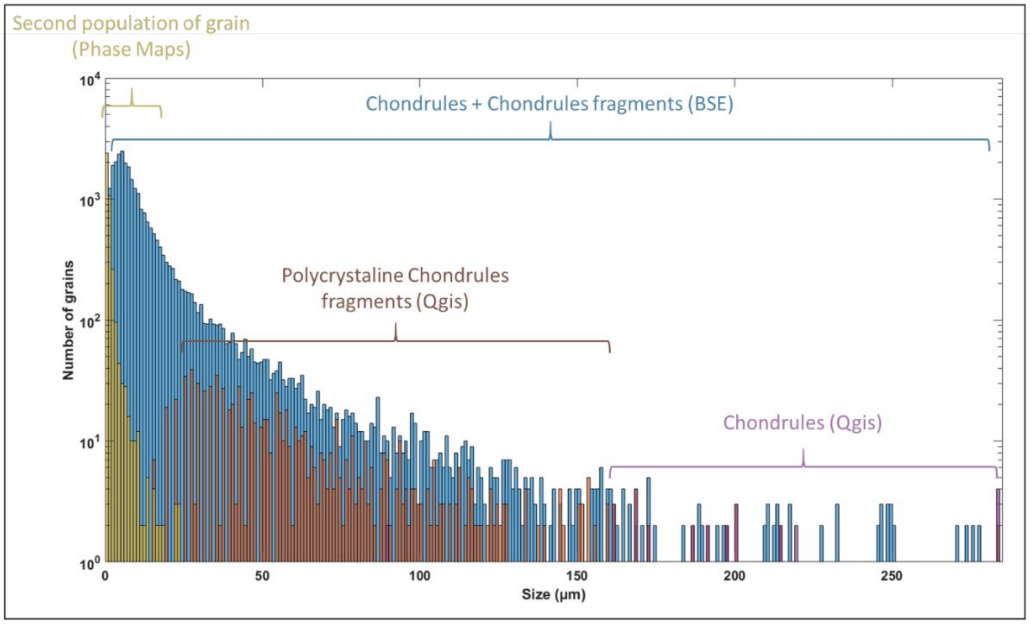

Size histogram of the anhydrous silicates. Chondrules and chondrule fragments from Qgis and the BSE mask draw a first population. Below 4 µm, another population associated with the silicate groundmass is evidenced.

5. Shape analysis

Here we show our results on the analysis of shape parameters of anhydrous silicate grains smaller than 4 µm. There is no clear distinction between the three populations.

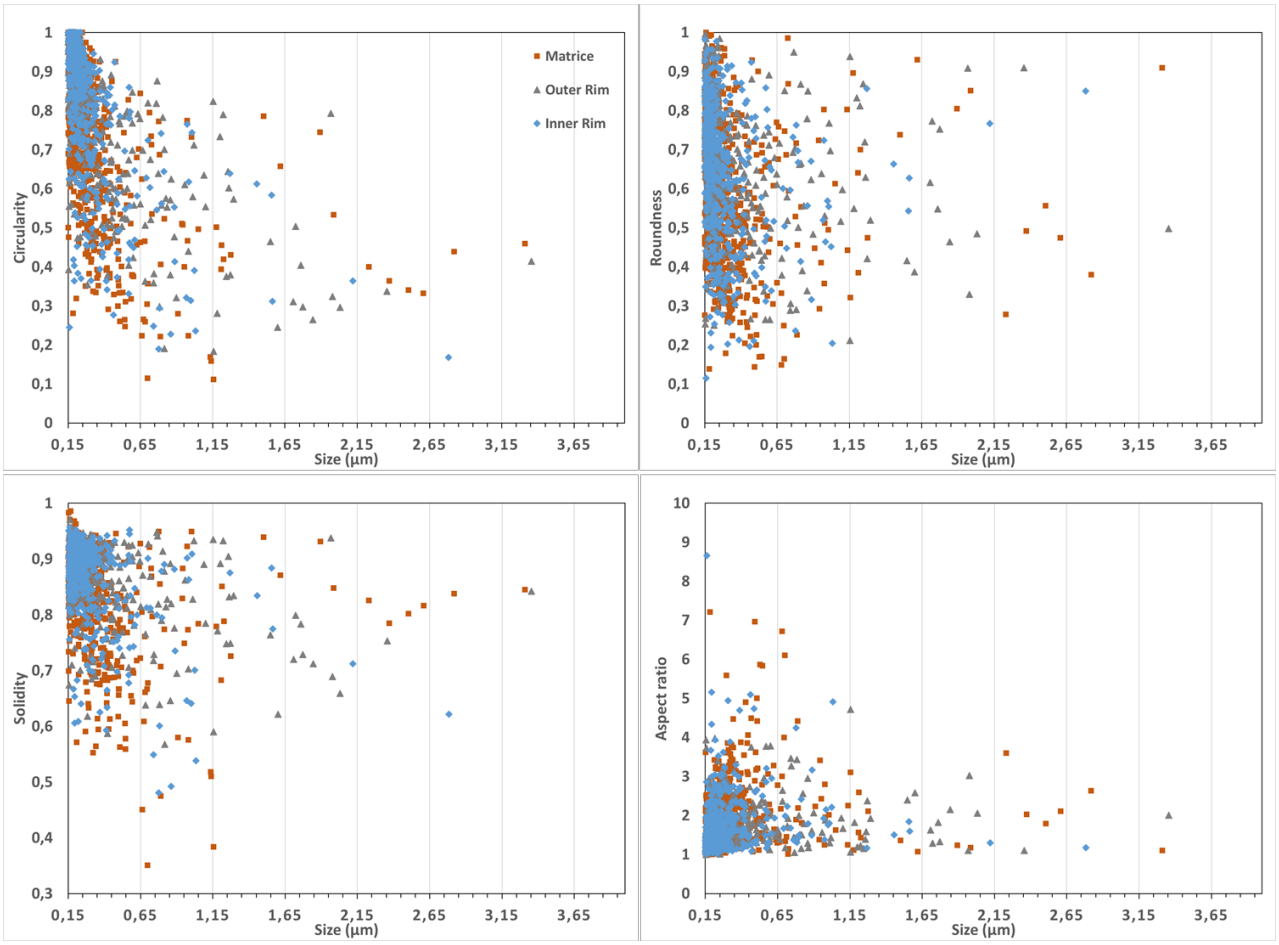

Plot of the shape parameters of the anhydrous silicate grains. Grains near to 1 are the more circular, round and do not show wide cavity for the first three plots. Grains with lower value exhibit more angular boundaries. The color represents the different region (matrix, inner and outer rim).

We based our grain shape analysis on four different shape factors: the circularity, the solidity, the aspect ratio and the roundness of the grains. Those four factors are described in the documentation of the software ImageJ (Ferreira et al., 2012). The circularity and the aspect ratio are more sensitive to the elongation while the roundness and the solidity are indicators of the sharp edges of the grains.

6. Tables of the normalized composition obtained from EPMA, ACADEMY and TEM.

	EPMA	Std dev	Matrix ACADEMY	abs. Err	Outer Rim ACADEMY	abs. Err	Inner Rim ACADEMY	abs. Err
Al	**1,26**	0,53	**1,35**	0,10	**1,12**	0,08	**1,15**	0,09
Ti	**0,79**	0,34	**1,09**	0,09	**1,09**	0,09	**1,08**	0,09
Ca	**0,30**	NA	**1,19**	0,09	**0,60**	0,04	**0,41**	0,03
Ni	**0,95**	0,59	**1,26**	0,10	**1,26**	0,10	**1,20**	0,09
Mg	**0,85**	0,36	**0,88**	0,06	**0,88**	0,06	**0,79**	0,06
Fe	**0,98**	0,35	**1,00**	0,07	**0,79**	0,06	**0,79**	0,06
Si	**1,00**		**1,00**		**1,00**		**1,00**	
Cr	**0,57**	0,23	**1,03**	0,04	**1,05**	0,04	**0,92**	0,04
P	**0,63**	0,42	**1,69**	0,17	**0,95**	0,10	**0,84**	0,09
S	**0,49**	0,37	**0,69**	0,05	**0,76**	0,06	**0,69**	0,05
K	**1,29**	0,63	**0,82**	0,07	**1,09**	0,09	**0,70**	0,06
Na	**0,66**	0,23	**0,43**	0,04	**0,57**	0,06	**0,32**	0,03

Table 1. Normalized ACADEMY compositions (SEM scale) of matrix and rims (average of all maps) plots as a function of 50% equilibrium condensation temperature in the least altered area. Data are normalized to Si and normalized to CI composition accordingly to (Lodders and Palme, 2009). EPMA data are obtained as described in (Hewins et al., 2014). Error are estimated based on the standard deviation of the multiple point analyses for the EPMA profile while they are calculated following the procedure explained in (Zanetta et al., 2019) for the ACADEMY results.

	EPMA	Std dev	Matrix ACADEMY	abs. Err	Outer Rim ACADEMY	abs. Err	Inner Rim ACADEMY	abs. Err
Al	**1,23**	0,91	**1,39**	0,11	**1,40**	0,11	**1,24**	0,09
Ti	**0,96**	1,04	**1,12**	0,09	**1,01**	0,08	**1,06**	0,08
Ca	**3,08**	NA	**1,49**	0,11	**0,53**	0,04	**0,54**	0,04
Ni	**0,77**	2,09	**1,74**	0,14	**1,47**	0,12	**1,46**	0,11
Mg	**0,83**	0,62	**0,75**	0,05	**0,78**	0,06	**0,78**	0,06
Fe	**0,92**	1,30	**1,22**	0,09	**1,23**	0,09	**1,09**	0,08
Si	**1,00**		**1,00**		**1,00**		**1,00**	
Cr	**0,51**	0,43	**0,91**	0,04	**1,00**	0,04	**1,03**	0,04
P	**0,48**	0,49	**0,99**	0,10	**0,63**	0,07	**0,57**	0,06
S	**1,03**	2,89	**0,81**	0,06	**0,77**	0,06	**0,61**	0,05
K	**1,38**	1,14	**1,01**	0,09	**1,21**	0,10	**1,28**	0,11
Na	**0,77**	0,80	**0,48**	0,05	**0,50**	0,05	**0,52**	0,05

Table 2. Normalized ACADEMY compositions (SEM scale) of matrix and rims (average of all maps) plots as a function of 50% equilibrium condensation temperature in the more altered area. Data are normalized to Si and normalized to CI composition accordingly to (Lodders and Palme, 2009). EPMA data are obtained as described in (Hewins et al., 2014). Error are estimated based on the standard deviation of the multiple point analyses for the EPMA profile while they are calculated following the procedure explained in (Zanetta et al., 2019) for the ACADEMY results.

	Matrix		Outer Rim		Inner Rim	
Al	**1,09**	0,41	**1,30**	0,31	**1,42**	0,21
Ti	**0,00**	2,48	**0,27**	2,02	**0,43**	1,44
Ca	**0,00**	0,16	**0,06**	0,10	**0,34**	0,07
Ni	**0,47**	0,25	**0,76**	0,21	**0,89**	0,14
Mg	**0,53**	0,06	**0,62**	0,05	**0,67**	0,03
Fe	**0,83**	0,07	**0,80**	0,05	**0,88**	0,04
Si	**1,00**		**1,00**		**1,00**	
Cr	**0,42**	0,61	**0,89**	0,51	**3,89**	0,34
P	**0,18**	2,39	**1,05**	1,43	**7,85**	1,01
S	**0,34**	0,10	**0,44**	0,08	**0,45**	0,05
K	**0,21**	2,04	**0,59**	1,79	**0,43**	1,31
Na	**0,87**	0,45	**0,81**	0,38	**0,80**	0,29

Table 3. Normalized compositions of the amorphous silicates extracted from the phase maps (at the TEM scale) plotted as a function of 50% equilibrium condensation temperature from (Lodders and Palme, 2009). Data normalized to Si and CI accordingly to (Lodders and Palme, 2009) in order to compare the S concentration.

7. Composition fields of the sulfide-rich and sulfide-poor regions.

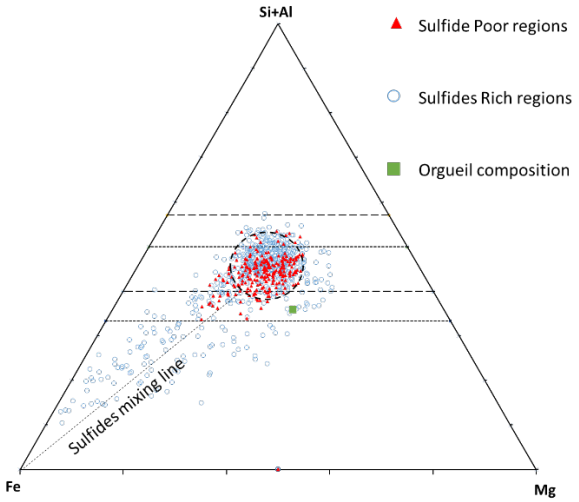

Fig. : Fe-Si+Al-Mg ternary diagram showing the composition fields of the sulfide-poor (red triangles) and the sulfide-rich (blue circles) of the inner rim.

The Figure shows that both the sulfide-poor and sulfide-rich regions share a similar cluster in composition, located between the serpentine and the pyroxene lines. This “endmember” represent the amorphous silicate. The composition of the amorphous silicate groundmass is similar for the two domain, as well as to the amorphous silicate groundmass of the matrix and the outer rim. The mixing line toward the sulfide “endmember” is only visible in the sulfide-rich domains.

8. Analysis of the more altered area

In the more altered lithology of Paris, inner and outer rims cannot be distinguished anymore in BSE imagery. The boundaries rims and matrix have been estimated by following the enrichment in anhydrous silicates (< 4 µm), present in the matrix but not in rims in the least altered lithology.

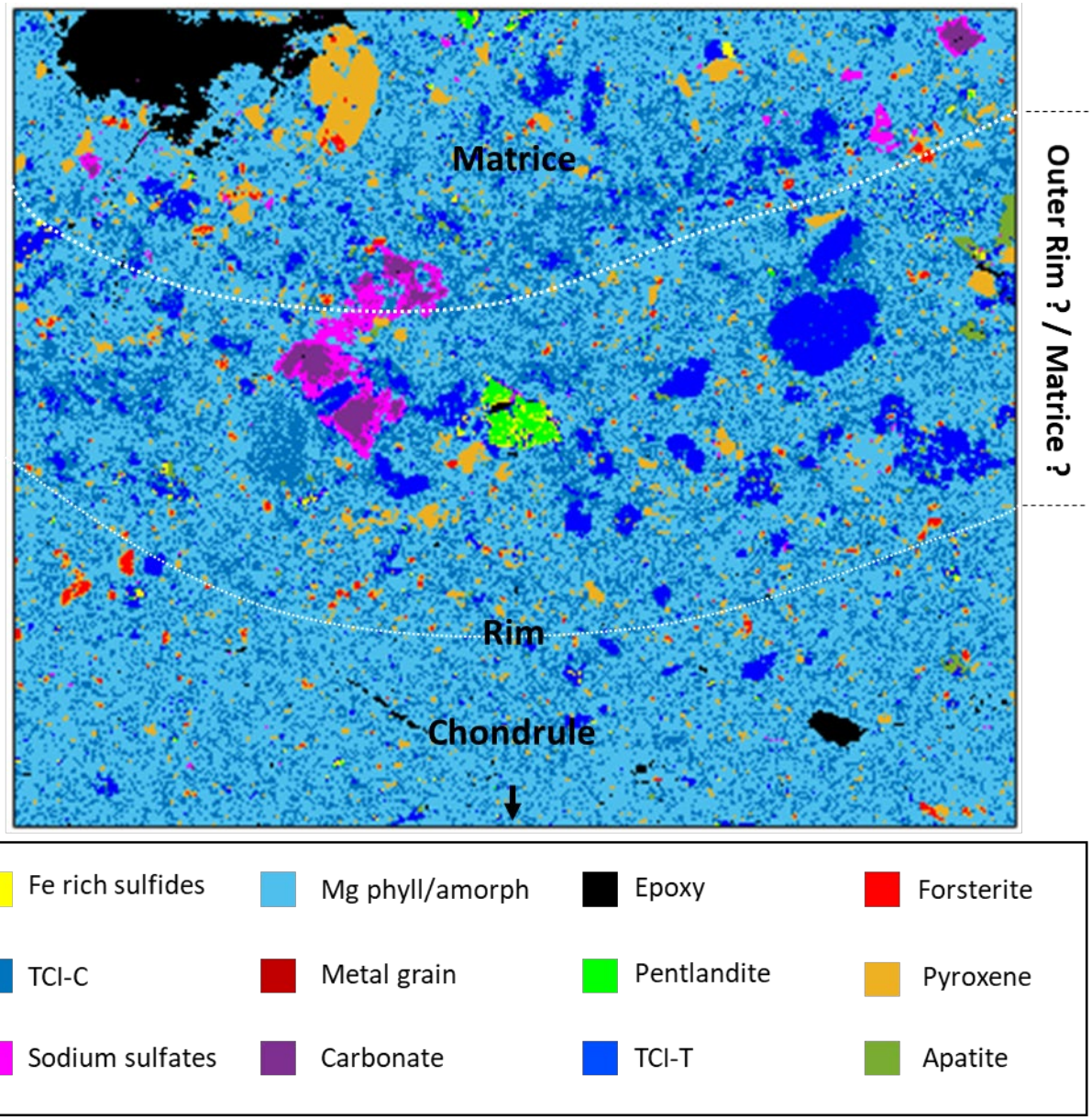

Phase map of an altered area. The distinction between the different regions (i.e. outer/inner rim and matrix) becomes more difficult.

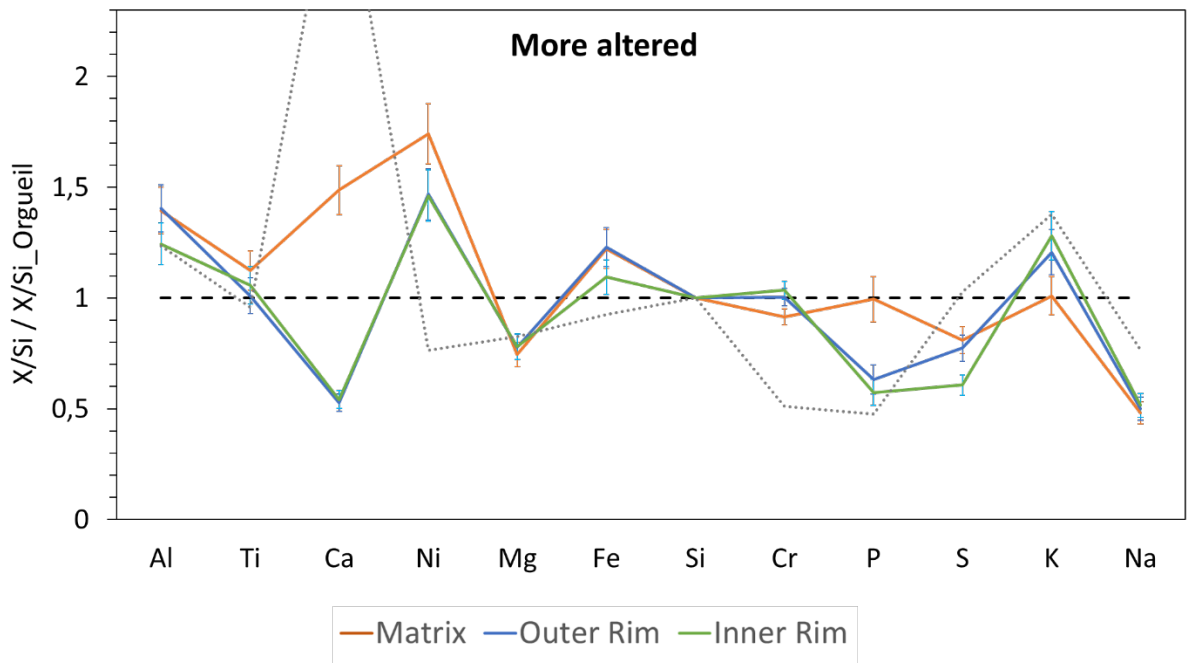

Comparison of the composition of the matrix and inner/outer rims in the more altered lithology of Paris. A hypothetical limit has been placed between the inner and the outer parts of the rim but the composition of the two zones are similar. Composition are normalized to Si and to Orgueil (Lodders and Palme, 2009).

Within the altered lithology, the alteration phases are abundant both in the matrix and in the rims. For instance, the abundance of TCI-T, which was almost absent in rims of the least altered lithology, is two times higher. Inversely, the anhydrous silicates are less abundant than in the least altered areas. The average composition in major elements of the rim is close to that of the matrix (Fig. above). Mg concentration is lower while Fe is higher, compared to the least altered lithology.

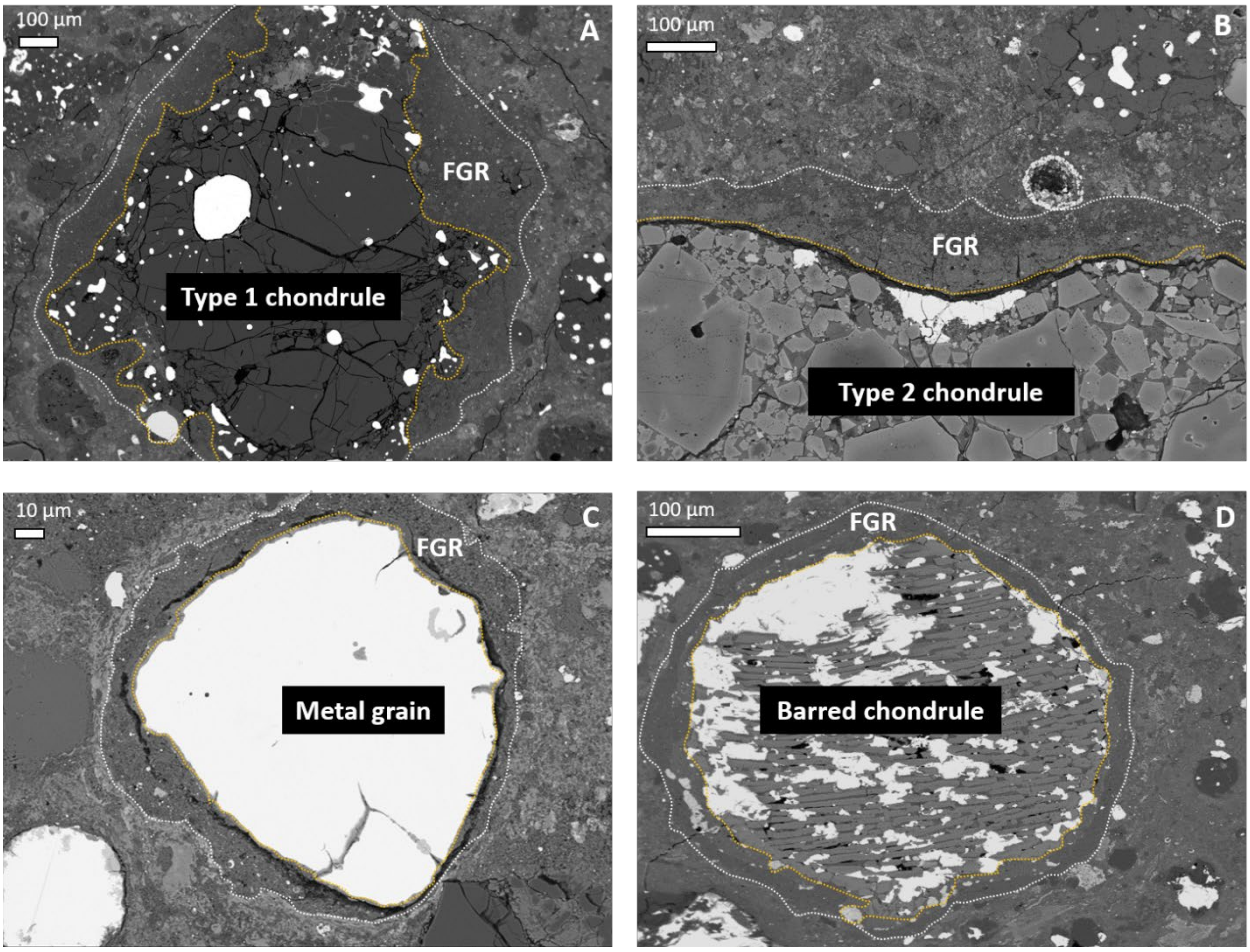

Figure 1 : FGRs surrounding different high temperature components. The orange line marks the contact with the components and the dashed white line represents the interface with the matrix.

	Non fragmented components			
	Area (%)	Number	Mean Radius (µm)	Rimmed fraction (%)
Type 1 chondrules	18.98	61.0	107.8	82.0
Type 2 chondrules	0.74	17.0	63.0	76.5
Non porphyritic chondrules	0.3	3.0	90.3	66.7
Metal grains	0.14	29.0	20.1	41.4
CAIs	0.02	9.0	47.0	88.9
Total	**20.18**	**119.0**		
	Fragments			
	Area (%)	Number	Mean Radius (µm)	Fraction rimmed (%)
Fragments	13.97	1083.0	29.6	<1.0

Table 1: Abundances and statistical counting of non-fragmented high temperature components obtained from BSE image analysis using QGis® (30 mm^2) in the least altered lithology.

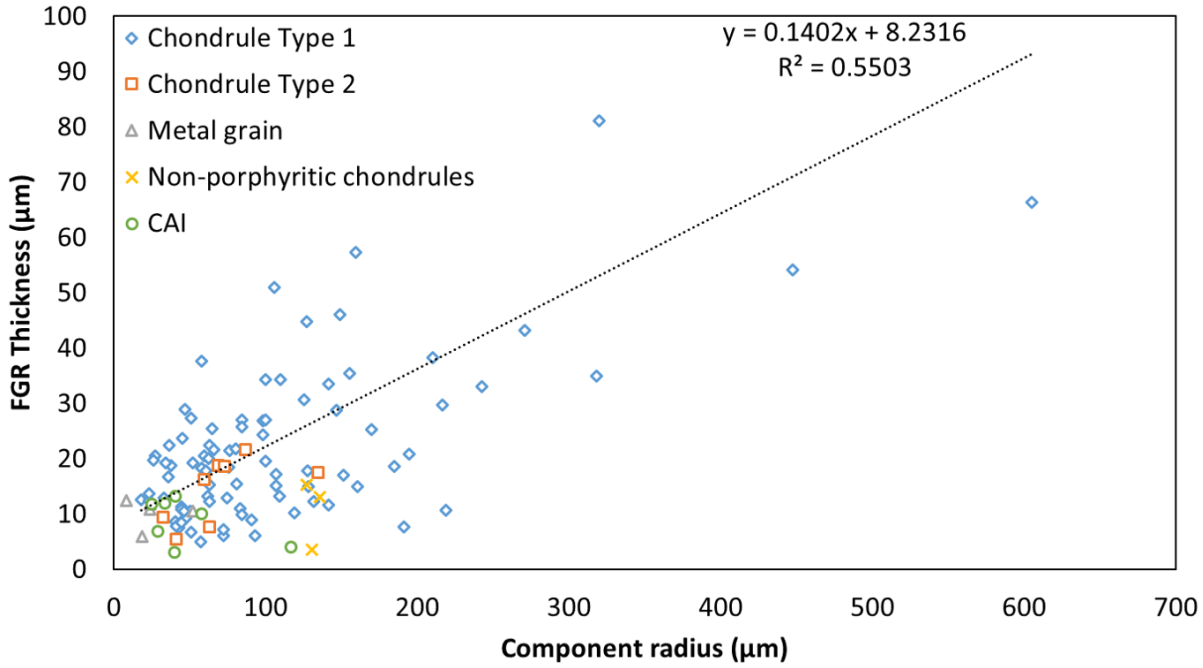

Figure 2 : Correlation between the apparent thickness of rims and the apparent radius of the rimmed component (i.e. chondrules, metal grain etc.).

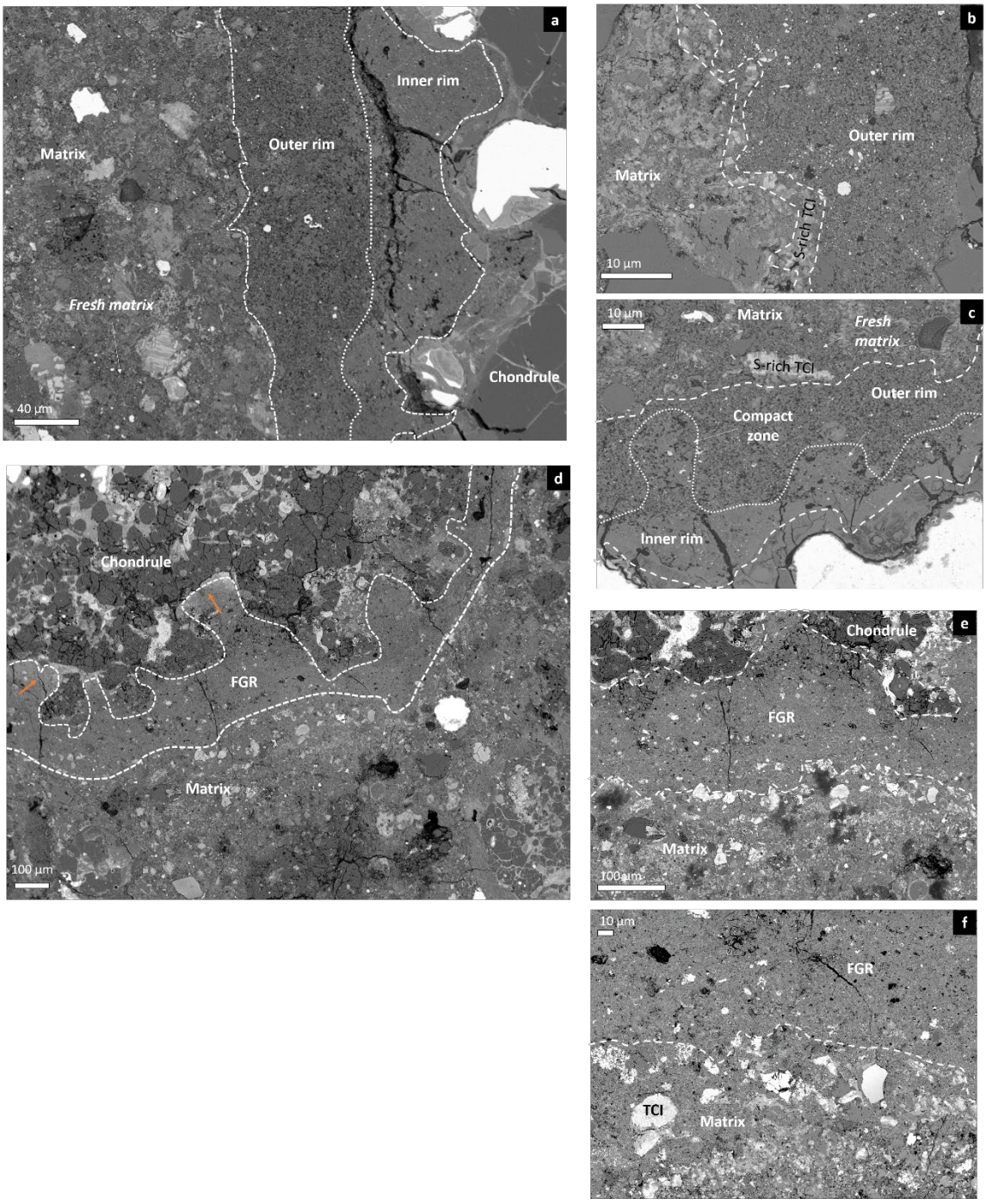

Figure 3 : BSE images of rimmed chondrules (a) Bilayer FGR surrounds a pristine type I chondrule in the least altered lithology. The chondrule exhibits large metal grains with thin oxidized edges. Pristine areas are visible in the matrix (darker). (b) Rim/matrix contact in the least altered lithology. Numerous TCI patches are present at the FGR- matrix boundary. The porosity of the outer rim and the contrast difference between the matrix and the rim are visible. (c) Complex porosity variations between the inner and the outer rim in the least altered lithology. (d) More altered lithology : the orange arrows show chondrule embayments. The rim appears thicker. (e) Chondrule/FGR/matrix interface in the more altered lithology. Differences delimiting an inner and an outer rim are not observed. (f) FGR texture in the more altered lithology : the material is more compact and homogeneous and exhibits small patches of TCI.

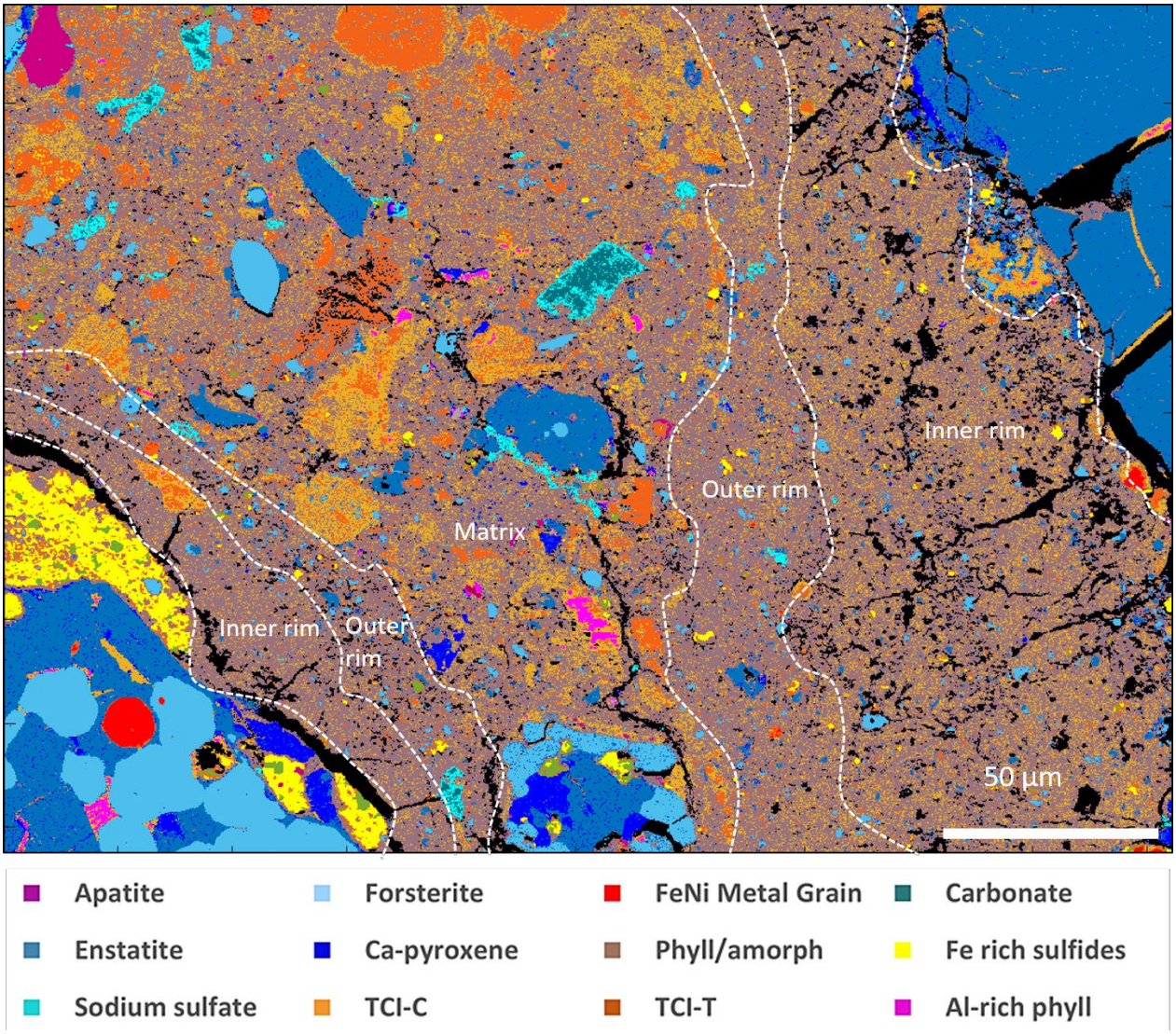

Figure 4: Phase map of two adjacent rimmed type I chondrules. The delimitations between outer rims and matrix and between inner and outer rims, based on BSE images, are outlined (dashed white lines).

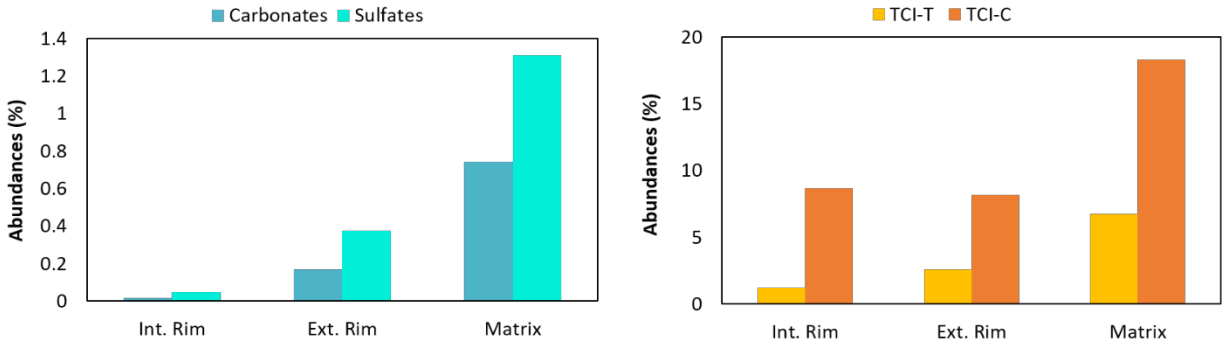

Figure 5 : Modal abundances of alteration phases (carbonates, sulfates and TCI) in matrix and rim. The matrix is enriched in these phases compared to the rims. The abundances of 3 maps are averaged.

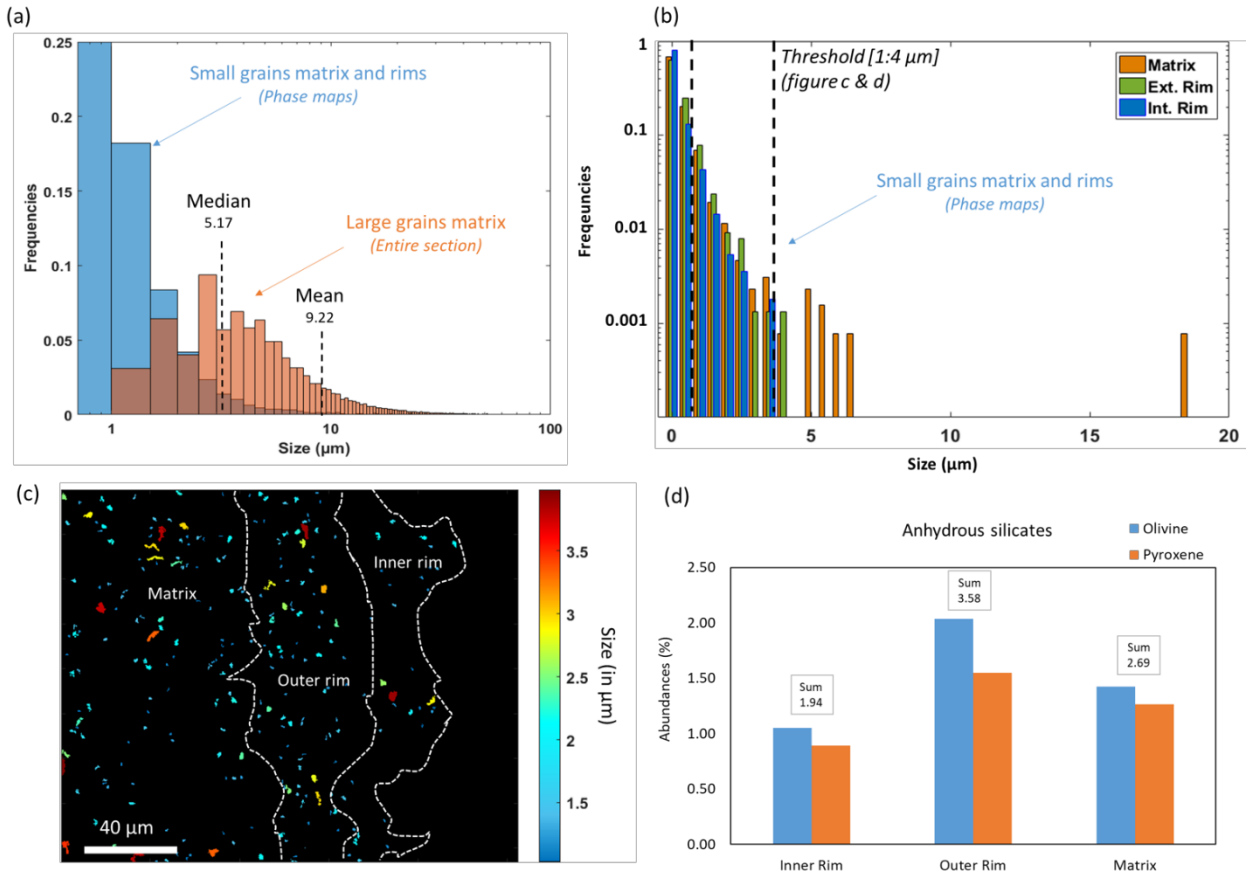

Figure 6: Statistical counting of anhydrous silicates in matrix and rims ***(a)*** *Grain size distribution of anhydrous silicates in matrix and rims. The diagram superimposes data obtained at high resolution from EDX phase maps (small grains) and at a larger scale from a BSE mosaic (for the larger grains). The brown part is where the populations overlap. The number of grains analyzed is 9380 for the high-resolution part and 76000 for the large-scale part; the areas probed are* $1.7.10^{-3}$ cm^2 *and 1* cm^2 *respectively. Frequencies are normalized between 0 and 1. The mean and median values are calculated from the section data.* ***(b)*** *Grain size distribution of anhydrous silicates in the outer rim, inner rim and matrix, based on high resolution phase maps. The dashed line represents the size threshold used for Fig. 6c and d. Largest grains (>4 µm) are in the matrix.* ***(c)*** *Phase map showing the spatial distribution of the grains with sizes smaller than 4 µm. The color bar indicates the grain size.* ***(d)*** *Modal abundances of anhydrous silicates below the 4 µm threshold (averaged based on the 3 phase maps). The outer rim exhibits significantly higher abundances.*

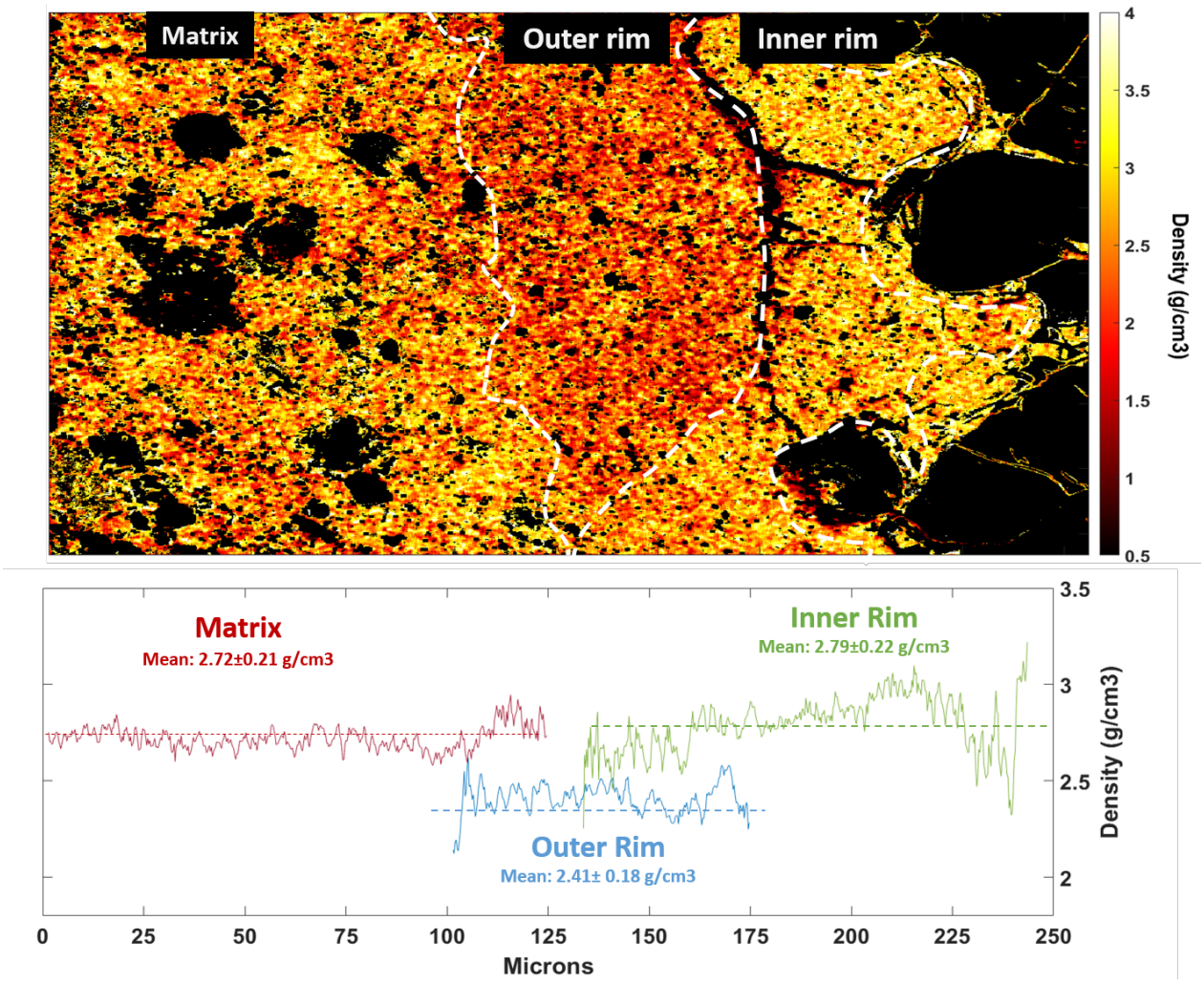

Figure 7 : Density map constructed using the background modelling from the ACADEMY method for a representative hyperspectral SEM-EDX map. Only the pixels that probe amorphous material/phyllosilicates with nano-inclusions are shown. The outer rim exhibits an apparent lower density while the bulk average compositions are similar in the matrix and in both rim portions. In the bottom part, the profile is a vertically averaged density value. First, a mask for each region (i.e. matrix, inner rim, outer rim) was extracted from the map in the top. Then pixels were vertically averaged for each column of the image and for each mask. Profile overlapping is due to the boundary of each region that does not coincide horizontally.

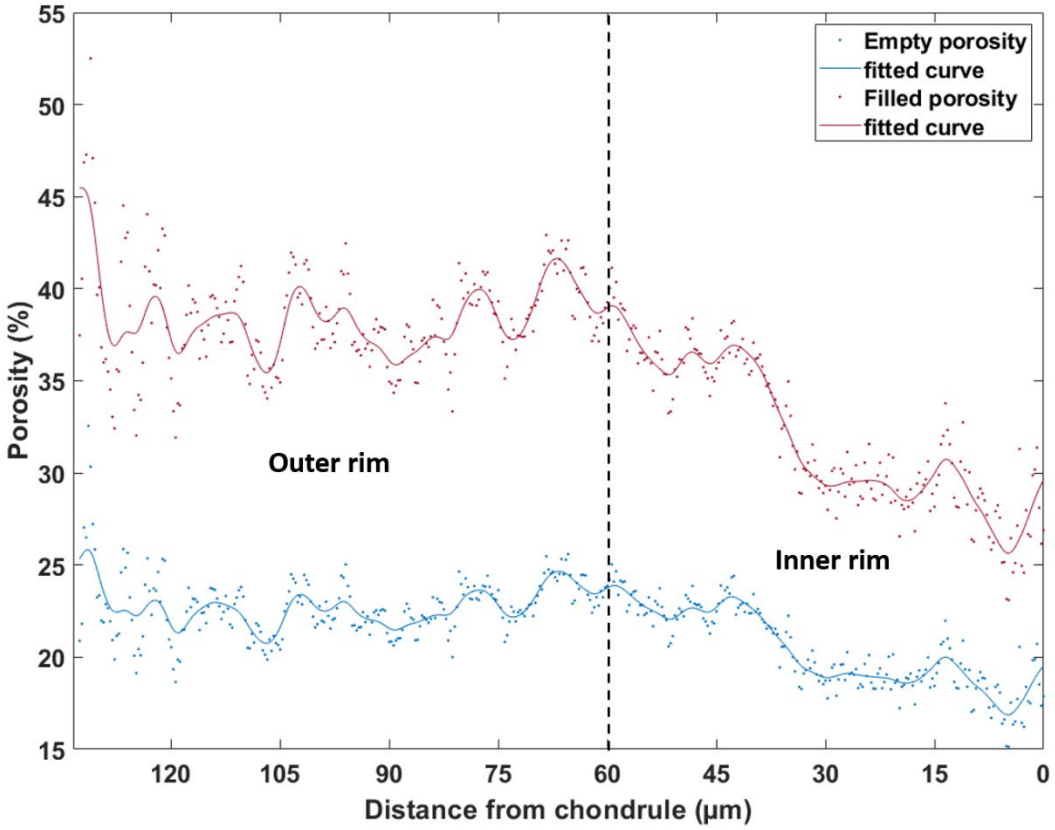

Figure 8 : Porosity distribution in rims deduced from density measurements. The blue data points are calculated assuming that the porosity is filled by an organic/epoxy -type material with density of 1.3 g/cm³. The orange data points are calculated assuming empty pores.

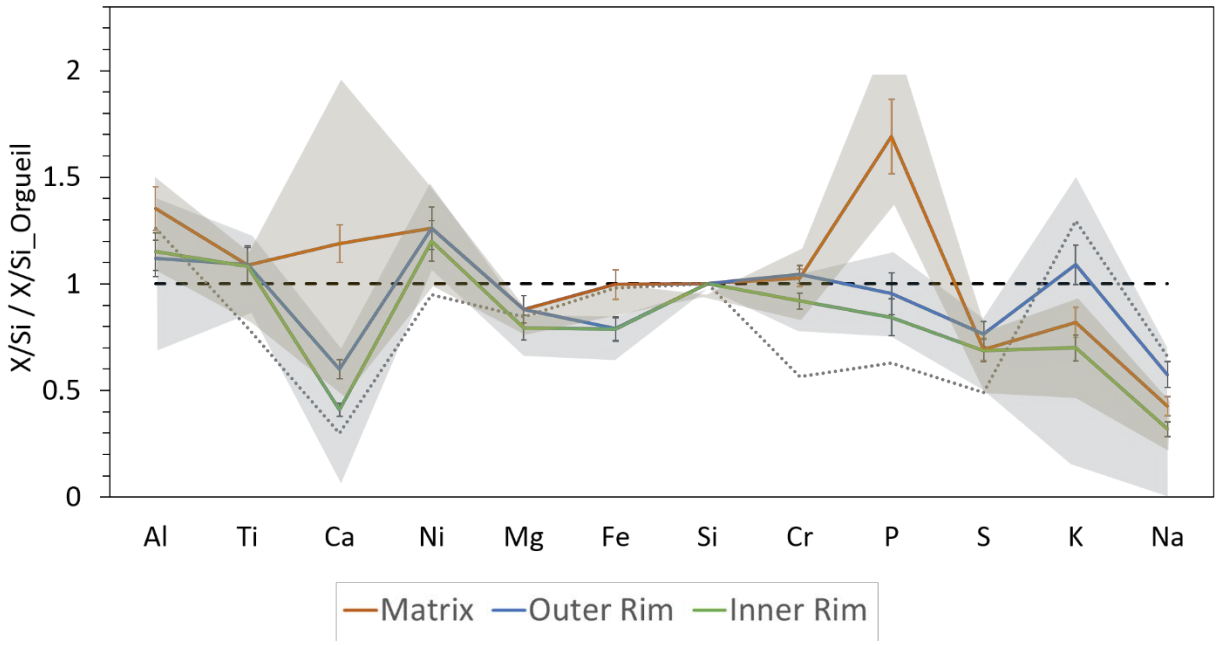

Figure 9 : Averaged composition, of matrix and rims, normalized to Si and chondritic composition (Lodders and Palme, 2009), deduced from the ACADEMY method. The elements are ordered following their 50% condensation temperature. Several phase maps are averaged for each lithology. Defocused EPMA data are shown for comparison (dotted line). The shaded regions represent the compositional variability of all maps (supplementary material 6). Elemental concentrations for all the three analyzed maps are comprised within shaded regions. The orange surface represents the variability of the matrix. The blue surface represents the variability observed both in inner and outer rim. Except for K and Na, the variability in the rims is low.

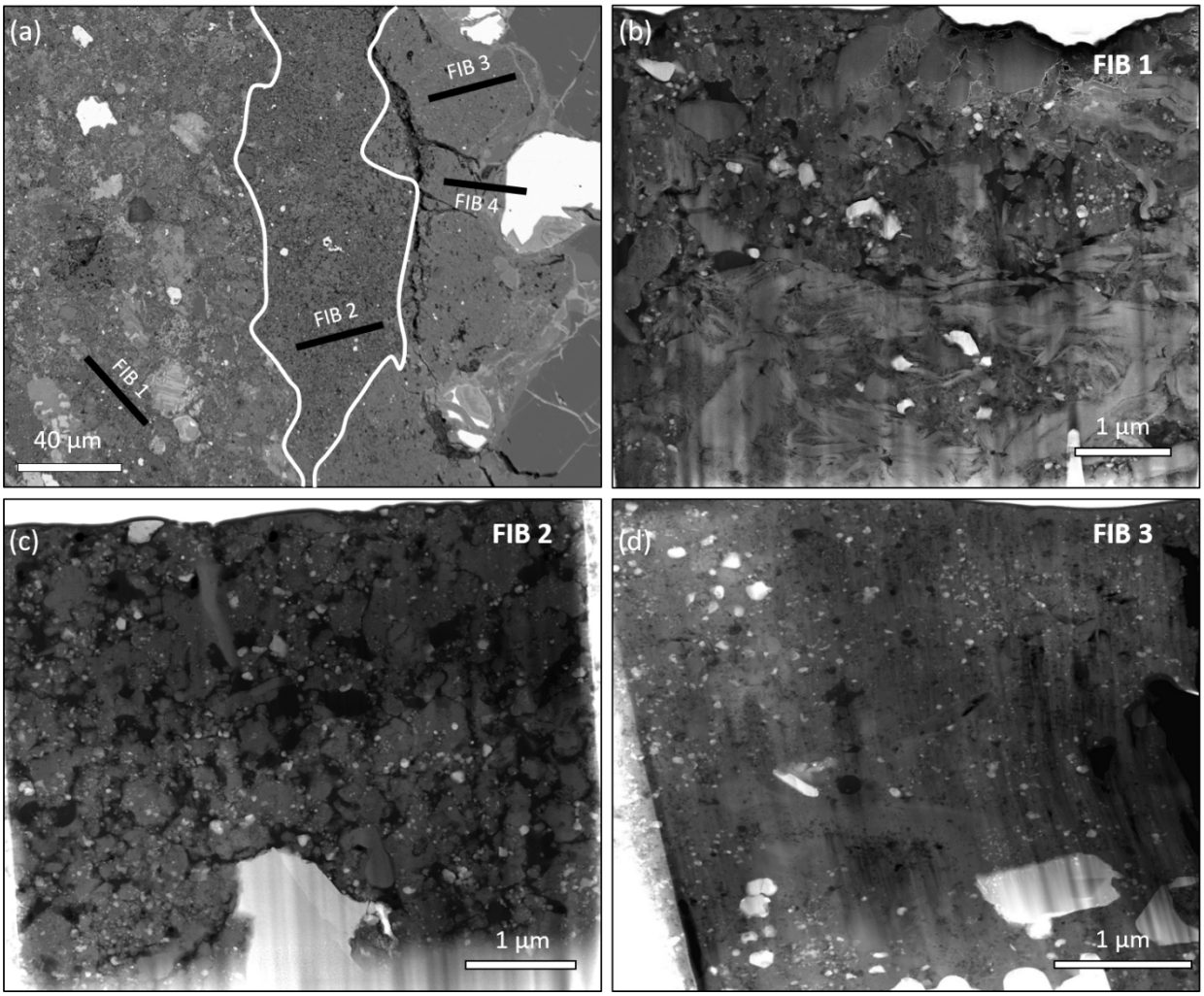

Figure 10 : STEM low magnification images of the matrix and rims (a) SEM-BSE image of the rimmed chondrule selected for the TEM study. The white line shows the limits of the outer rim. The location of the extracted FIB sections is indicated. (b, c, d) HAADF-STEM low magnification view of sections extracted in the matrix and the two portions of the rim. The FIB 1 is samples the darkest and most porous areas of the matrix based on the SEM-BSE image, FIB 2 was extracted in the outer rim and the FIB 3 in the inner rim.

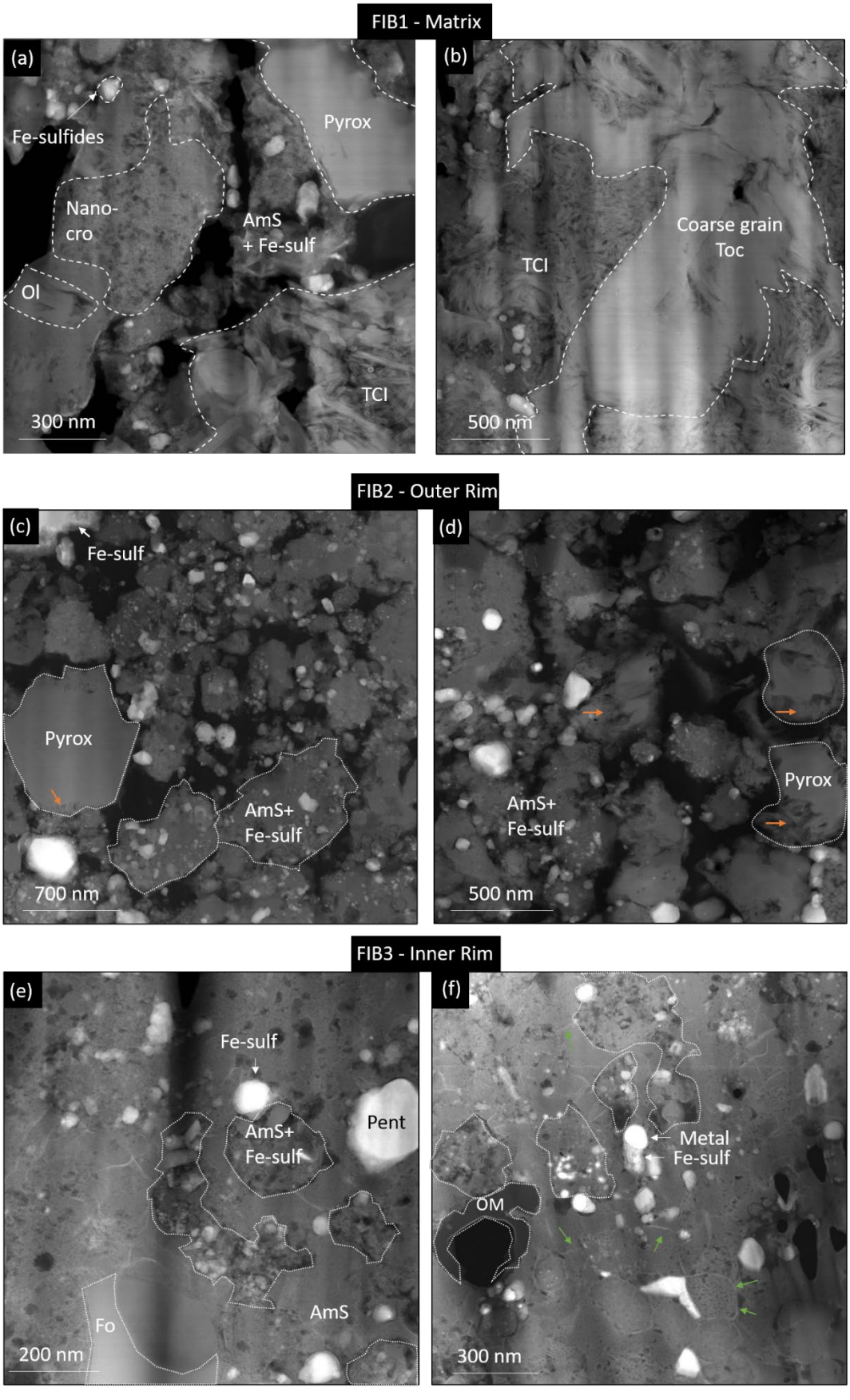
FIB1 - Matrix
(a)
Fe-sulfides
Pyrox
Nano-
cro
AmS
+ Fe-sulf
Ol
TCI
300 nm
(b)
Coarse grain
Toc
TCI
500 nm
FIB2 - Outer Rim
(c)
Fe-sulf
Pyrox
AmS+
Fe-sulf
700 nm
(d)
Pyrox
AmS+
Fe-sulf
500 nm
FIB3 - Inner Rim
(e)
Fe-sulf
AmS+
Fe-sulf
Pent
AmS
Fo
200 nm
(f)
Metal
Fe-sulf
OM
300 nm

Figure 11: STEM-HAADF images the matrix, the outer and the inner rim. (a) Matrix: Fibrous phyllosilicate areas next to amorphous silicate domains associated with nanosulfides. (b) Matrix: Coarse-grained tochilinite surrounded by nanometric sheets of cronstedtite intermingled with tochilinite. (c) Outer rim: individual domains of amorphous silicates bearing nanosulfides (two of them are delineated), separated by porosity. (d) Outer rim: detail of the amorphous silicate associated with nanosulfides. The orange arrows point to rare signs of alteration of the pyroxene grains. (e) Inner rim: amorphous silicate domains bearing abundant sulfides, surrounded by a smooth, homogeneous, texturally continuous and sulfide-poor amorphous silicate. (f) Inner rim: compact sulfide-poor and sulfide-rich domains showing low porosity. A few metal grains are present. The green arrows indicate Fe-enriched (high Z) surfaces. The abbreviations are: Fo = forsterite, ol=olivine with Fe-content between 5 and 10 %, Nanocro = nanocrystalline cronstedtite, AmS+Fe-sulf = amorphous silicates associated with nanosulfides, Toc = tochilinite, TCI = tochilinite-cronstedtite intergrowth, Fe-sulfides= Fe-rich sulfides (i.e. troilite or pyrrhotite), Pent= Pentlandite, Pyrox= pyroxene.

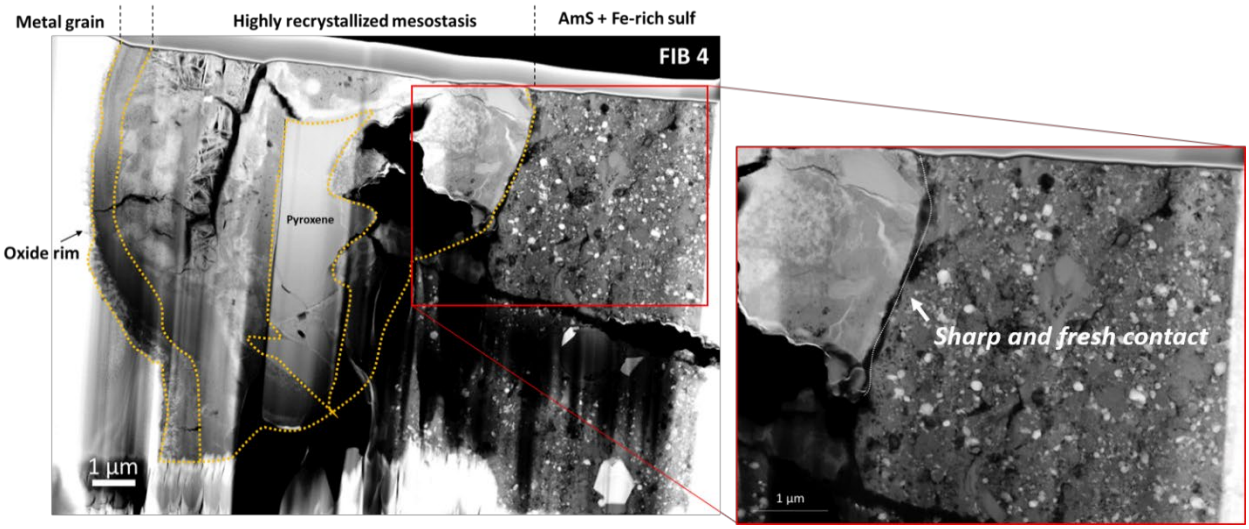

Figure 12: HAADF images of the contact between the chondrule (left) and the inner rim (FIB 4). The yellow lines delineate the mesostasis. Phyllosilicates are visible and surround a pyroxene crystal. Detail of the chondrule/inner rim interface: the contact is sharp, and the rim material does not seem to be more processed at the interface

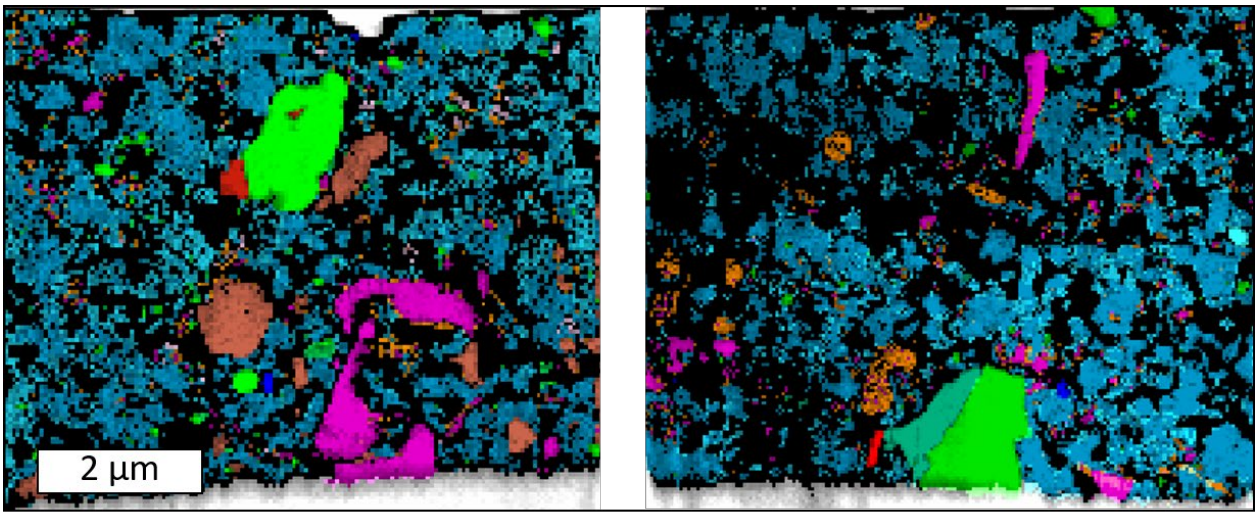

Figure 13 : Phase map on the outer rim FIB 2 section obtained by MLLS fitting We considered two population of amorphous silicate to better take into account and fit its variable composition, which is highly variable for the Mg/Fe ratio.

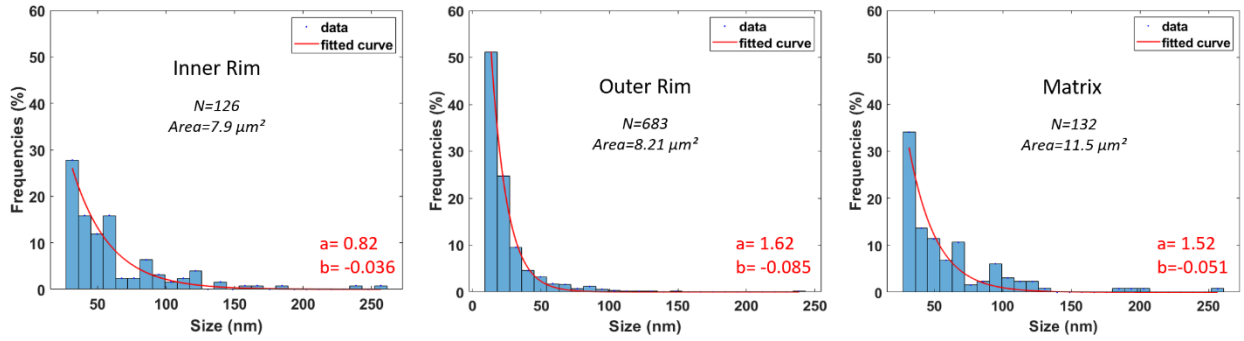

Figure 14 : Size distribution of the sulfides associated with amorphous silicates. Each histogram is fitted with an exponential curve: $y = a * exp(b * x)$. The fitted parameters are indicated in red. N is the number of grains. The size of the analyzed area is also indicated.

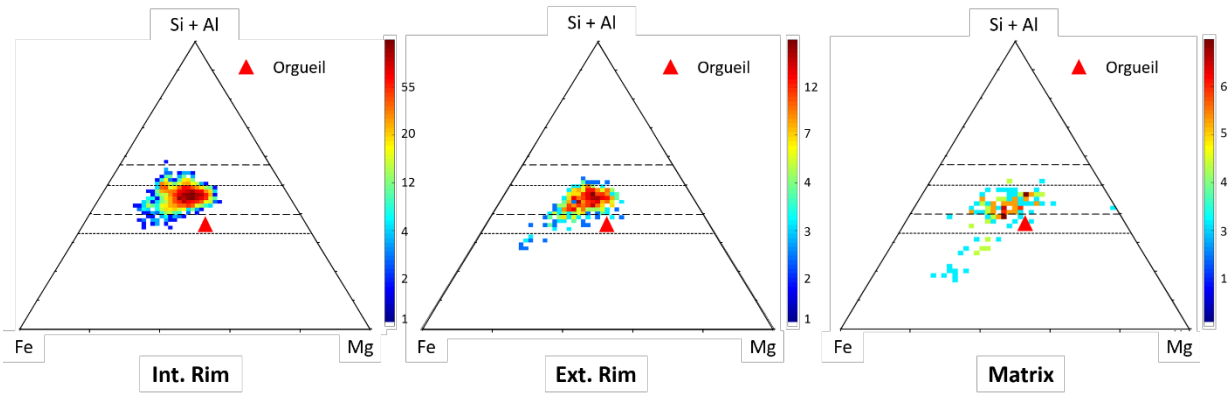

Figure 15 : Fe-Mg-(Al+Si) ternary diagrams (at.%) showing the composition field of the amorphous silicates in the matrix, the outer rim and the inner rim. The colorbar indicates the number of data within a given compositional range (point density; triplot module of XmapTools (Lanari et al., 2014)). The chondritic composition (Orgueil (Barrat et al., 2012)) is indicated by a black circle. The lines (from the bottom to the top) represent the solid solutions for olivine, serpentine, pyroxene, saponite.

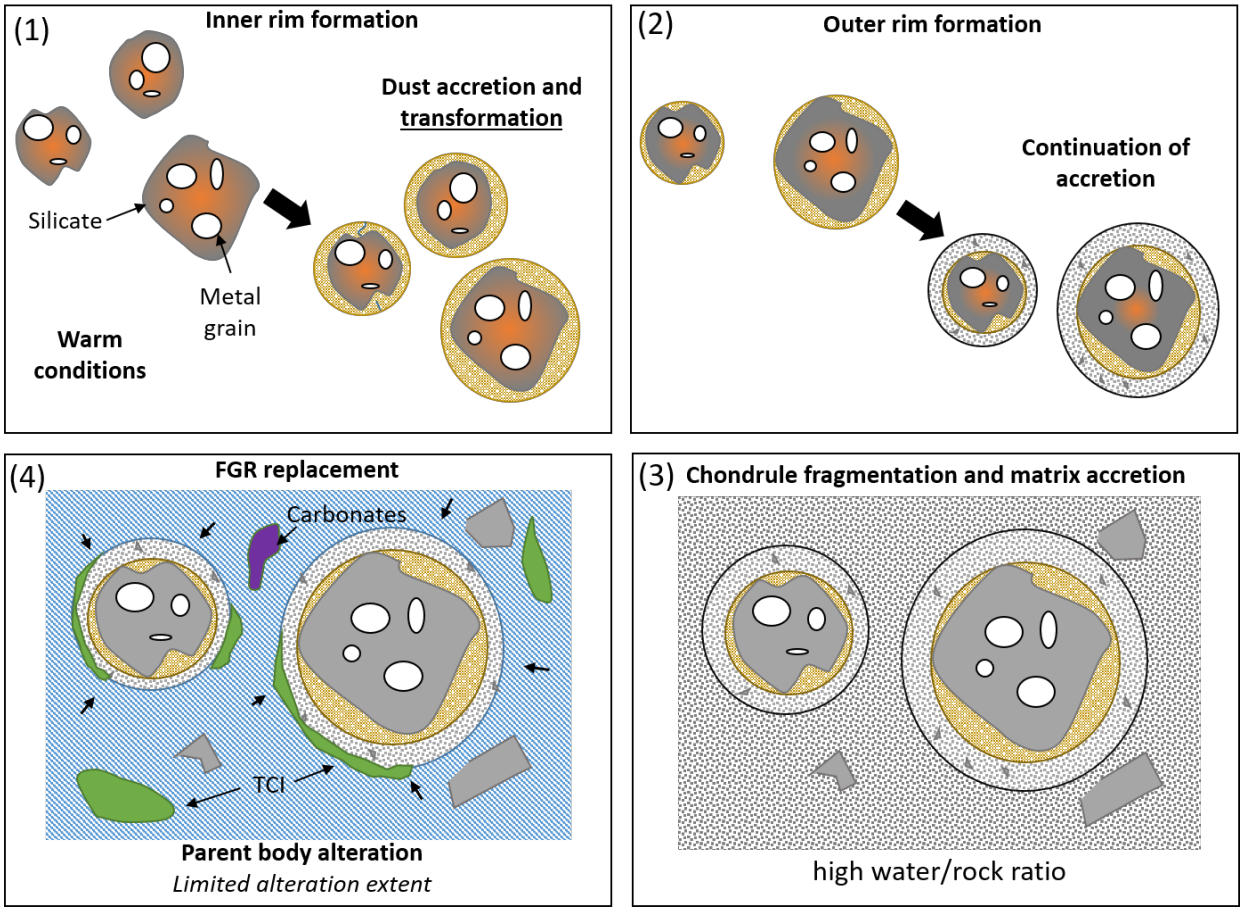

Figure 16 : Schematic representation describing the steps that led to the present state of the Paris chondrite. FGRs are formed in a nebular environment through the accretion of dust onto chondrules. The matrix is accreted after in a colder environment with additional chondrule fragments. A differential alteration occurred due to the initial difference in water/rock ratio.